Diagenetic products, settings and evolution of the pre-salt succession in the Northern Campos Basin, Brazil

Michael Strugale[1]*, Bruno Eustáquio Moreira Lima[2], Christopher Day[3], Jenny Omma[4], Jeremy Rushton[5], João Paulo Roncolatto Olivito[6], Jon Bouch[7], Laurence Robb[3], Nick Roberts[5] and Joe Cartwright[3]

[1]E&P Reservoirs, Petrobras S.A., Rio de Janeiro, Brazil

[2]E&P Búzios, Petrobras S.A., Rio de Janeiro, Brazil

[3]Department of Earth Sciences, University of Oxford, Oxford, UK

[4]Rocktype Ltd, Oxford, UK

[5]British Geological Survey, Keyworth, UK

[6]E&P Ultra-deep Waters, Petrobras S.A., Santos, Brazil

[7]Pore Scale Solutions Ltd, Carwynnen, UK

MS, 0000-0003-1106-7529; BEML, 0000-0003-0000-0636; JO, 0000-0003-3265-2719; JR, 0000-0001-5931-7537; LR, 0000-0002-9032-1320; NR, 0000-0001-8272-5432; JC, 0000-0003-4198-9719

*Correspondence: michael_strugale@petrobras.com.br

Abstract: Despite all the effort made towards an understanding of the sedimentary, tectonic and diagenetic evolution of the pre-salt sequence and the Pre-Salt reservoirs of the Northern Campos Basin (East Brazil), two knowledge gaps have yet to be filled: (1) a detailed study of diagenesis in the crystalline basement and rift phases; and (2) the timing of diagenetic events that affected the pre-salt succession. In this study, samples from these geologic units were analysed for mineral composition and paragenetic evolution, fluid temperature and salinity, stable isotope compositions and laser ablation inductively coupled plasma mass spectrometer derived U–Pb ages of carbonate phases. The U–Pb ages of replacive and vein-filling cements reveal three tectono-diagenetic events, named the Barremian–Aptian (BADE, 125–117 Ma), the Albo–Cenomanian (ACDE, 103–98 Ma) and the Campanian–Maastrichtian (CMDE, 83–70 Ma). Each phase is characterized by distinct minerals, precipitation temperatures and burial conditions. The hydrothermal qualifier, identified by the temperature contrast between fluid and host rock, was initially high during BADE, then diminished over time (through ACDE) until it achieved equilibrium with the host rocks during CMDE. Diagenetic events are not coeval with magmatism but do coincide with known regional tectonic events described in the literature and are interpreted to be the result of increasing intraplate stresses. Multidisciplinary studies that include diagenetic events constrained by geochronological data will certainly lead to more robust conceptual geologic models, and, therefore, to a more reliable management of resources and strategies such as enhanced oil recovery, carbon capture, utilization and storage, and drinking water.

Supplementary material: Supporting petrographic, QEMSCAN and CL imagery, detailed description of the fluid inclusions, the analytical procedures and the complete results of LA-ICP-MS U–Pb geochronology are available at https://doi.org/10.6084/m9.figshare.c.7103900

Secondary porosity formed by hypongenic karstification of hydrothermal origin is of fundamental importance in the oil and gas industry, the mining industry and in studies of shallow groundwater circulation in the environmental industry (Corbella *et al.* 2004; Loucks *et al.* 2004; Davies and Smith 2006; Klimchouk 2015; Parise *et al.* 2018). The term 'hydrothermal' in this study refers to waters that are warmer (>5–10°C) than the surrounding environment (White 1957; Machel and Lonnee 2002; Davies and Smith 2006). Speleogenesis, brecciation, dolomitization, silicification, dissolution and 'exotic' minerals that include Mississippi Valley-type (MVT) Zn–Pb ores observed in several geological contexts are the products of hydrothermal diagenesis (Hesse 1989; Davies and Smith 2006; Neilson and Oxtoby 2008). Therefore, hydrothermal diagenesis is a process related to hypongenic karstification and characterized as a succession of events including speleogenesis (i.e. generation of secondary porosity by dissolution) and pore filling, which often work selectively within structures and rock strata (Klimchouk 2012).

The Macabu Formation and the upper part of the Coqueiros Formation constitute the Pre-Salt

From: Garland, J., Barnett, A. J., Burchette, T. P. and Wright, V. P. (eds) 2025. *Carbonate Reservoirs: Applying Current Knowledge to Future Energy Needs*. Geological Society, London, Special Publications, **548**, 231–265.
First published online April 26, 2024, https://doi.org/10.1144/SP548-2023-93

reservoirs in the Northern Campos Basin (SE Brazil; Winter *et al.* 2007; Herlinger *et al.* 2017). They represent the post-rift (PR) and rift transition (RTR) stages of the basin, respectively, and were deposited during Barremian times (Tedeschi *et al.* 2019; Olivito and Souza 2020; Pietzsch *et al.* 2020). The analysis of the petrographic, depositional, stratigraphic, geochemical and palaeothermometric properties of these reservoirs revealed a significant hydrothermal influence during diagenesis as a result of magmatic events under deep burial conditions (Herlinger *et al.* 2017; Lima and De Ros 2019; Lima *et al.* 2020; Olivito and Souza 2020). Recently, this area was re-examined in terms of basement geology and its influence on the structural style of the faults that affected the overlying rift sediments (Strugale *et al.* 2021). Furthermore, Strugale and Cartwright (2022) proposed a comprehensive tectonostratigraphic evolution model for the entire pre-salt sequence, recognizing two episodes of rifting followed by selective PR inversion. Finally, the formal stratigraphic column of the pre-salt sequences (cf. Winter *et al.* 2007) was constrained by new depositional ages (Tedeschi *et al.* 2017; Tedeschi *et al.* 2019; Pietzsch *et al.* 2020; Sanjinés *et al.* 2022). Importantly, there is no geochronological constraint for the diagenetic events of the entire pre-salt sequence, and the characterization and diagenetic phases of the basement and the rift phases remain poorly understood.

The diagenesis observed in rocks submitted to a relatively simple, continuous burial history with a few disturbances by magmatic events, such as the pre-salt sequence of the Campos Basin, still exhibits a quite complex paragenetic sequence (Lima and De Ros 2019; Lima *et al.* 2020). The relative timing of mineral formation is often difficult to establish in thin sections because it is characterized by an alternation of similar minerals, suggesting episodes of *in situ* dissolution and precipitation which can be attributed to diffusion (Pingitore 1982). Fracturing and subsequent filling in deep burial contexts are much more continuous in time and have strong feedback with rock and fluid chemistry (Laubach *et al.* 2019) despite the lack of absolute ages to attest this interpretation. Fortunately, U–Pb geochronology through laser ablation inductively coupled plasma mass spectrometer (LA-ICP-MS) in carbonates has become widely used, with emphasis on dating diagenetic and brittle deformation events recorded in carbonate cements (Roberts *et al.* 2020; Rochelle-Bates *et al.* 2021; Ganade *et al.* 2022).

The aims of this work are to:

- Describe the host rocks, diagenetic products and paragenetic evolution of the syn-rift and RTR sediments, and the Precambrian basement;
- Characterize the diagenetic mineral phases in terms of constitution, composition, absolute ages, carbon ($\delta^{13}C$) and oxygen ($\delta^{18}O$) stable isotopes, palaeotemperatures and fluid salinity;
- Depict the diagenetic environments and build a time-constrained model for the diagenetic evolution of the Campos Basin and associated tectonic and magmatic events.

Geological context

The study area is located 70 km offshore in the deep-water context of the Northern Campos Basin, East Brazil. It overlies a basement comprising the transition zone between the Cabo Frio Tectonic Terrain (CFTD; cf. Schmitt *et al.* 2004) and the Oriental Terrane of the Ribeira Belt, with both units having been involved in the Brasiliano orogenetic tectonic events of Ediacaran–Cambrian age (Schmitt *et al.* 2016; Stanton *et al.* 2019; Strugale *et al.* 2021) (Fig. 1a). The Campos Basin formed by rifting of West Gondwana during the Early Cretaceous (Rabinowitz and LaBrecque 1979; Chang *et al.* 1992) and evolved during an initially magma poor, then magma-rich, break-up stage (Morgan *et al.* 2020).

Extensional tectonics of rift phase 1 (RP1) probably started during the Berriasian and reached its peak during rift phase 2 (RP2; the Hauterivian). RP1 resulted in the formation of isolated NNE–SSW-trending, east–west stacked grabens filled with volcaniclastics and coarse arkoses of the Cabiúnas, Itabapoana and Atafona formations. RP1 faults were reactivated and new faults were nucleated during RP2, resulting in extensive NE–SW half-graben development that fringes a 10 km-wide regional horst (the Guriri Fault System–GFS). The grabens of RP2 were initially filled with reworked carbonates and hybrid laminites in the depocentres, followed by bioclastic rudstones (coquinas deposits) stacked onto the structural highs and transitioning to lower energy facies towards the depocentres (Strugale and Cartwright 2022). These units correspond to the lower section of the Coqueiros Formation (Coq A; Olivito and Souza 2020; Fig. 1b).

The upper section of the Coqueiros Formation is interpreted as a RTR phase. Olivito and Souza (2020) subdivided the RTR into three sets of facies associations and organized them into four seismic-stratigraphic units (Coq B–E; Fig. 1b). Coq B–D represent an overall coarsening-up sequence on which bioclastic rudstones and grainstones are the main porous facies. On the other hand, Coq E represents a restricted, evaporative environment with a higher clay content. The overlying Macabu Formation was deposited during the PR stage in a highly evaporative alkaline lacustrine system (e.g. Muniz and Bosence 2015; Lima and De Ros 2019; Pietzsch *et al.* 2020). Following a gap, whose duration is under debate, extensive deposition of marine-

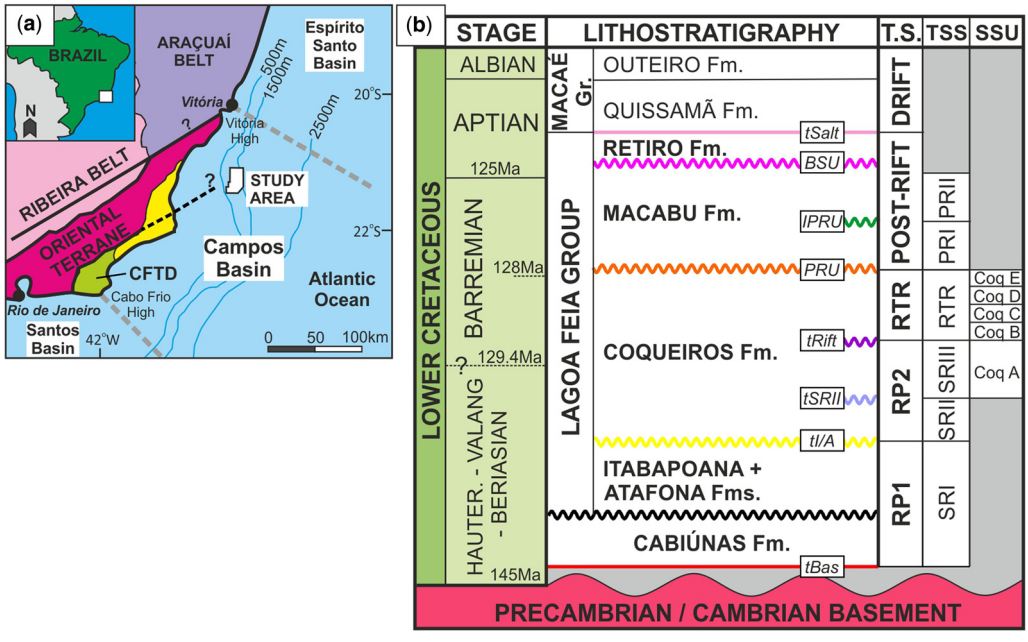

Fig. 1. (**a**) Location of the studied area and simplified geological map of the onshore basement. (**b**) Stratigraphic framework of the studied area. Stages are based on Strugale and Cartwright (2022) and references therein. Lithostratigraphy is based on Winter *et al.* (2007), where the horizons tSalt (top salt), BSU (base salt unconformity), IPRU (internal PRU), PRU (post-rift unconformity), tRift (top rift), tSRII (top SRII), tI/A (top Itabapoana/Atafona formations), and tBas (top basement) are the mapped seismic horizons. Tectonic stages (T.S.) are based on Strugale and Cartwright (2022) and Winter *et al.* (2007). Tectonicstratigraphic sequences (TSS) are as defined in Strugale and Cartwright (2022). Seismic-stratigraphic subdivisions (SSU) of the Coqueiros Formation are as proposed in Olivito and Souza (2020). CFTD: Cabo Frio Tectonic Domain (cf. Schmitt *et al.* 2004); Fm; formation; PRI and PRII, post-rift sequences I and II, respectively; RP1 and RP2, rift phases 1 and 2, respectively; RTR, rift transition stage; SRI, SRII and SRIII, syn-rift phases I–III, respectively.

derived evaporites of the Retiro Formation took place during the Aptian, followed by shallow-marine carbonates of the Quissamã Formation (Winter *et al.* 2007; Sanjinés *et al.* 2022). The deposition of Quissamã carbonates triggered widespread thin-skinned gravitational gliding of salt and related salt compression in the outer regions of the Campos Basin (Davison 2007; Szatmari *et al.* 2021).

The pre-salt sequence corresponds to the sedimentary and volcanic rocks bounded by the crystalline basement at the base and the evaporite layer on the top. In other words, it includes the geological formations encompassed in the Lagoa Feia Group, except for the Retiro Formation (evaporites) and the basal Cabiúnas Formation (Fig. 1b). This specific terminology was used by Strugale *et al.* (2021) and Strugale and Cartwright (2022) because they were the first to study an area on which the crystalline basement was drilled, thus the entire pre-salt succession was investigated. On the other hand, the Pre-Salt reservoir has an extensive usage in the literature to refer to the RTR to the PR units comprising the Macabu and the upper Coqueiros formations, respectively, in the Campos Basin, and their equivalents in the counterpart Santos Basin (the Itapema and Barra Velha formations, respectively) (Carminatti *et al.* 2008; Muniz and Bosence 2015; Fetter *et al.* 2018).

Materials and methods

This study is based on 67 sidewall cores from 18 wells (Fig. 2). The strategy for sample selection aimed to obtain novel data for RP1 and the Precambrian basement, and to investigate samples of RP2 and RTR tectonic stages which could represent end-members of the most diagenetically altered rocks. In these samples, the layering is blurred and features such as vugs, fractures and brecciation are common. Therefore, they are distinct from those in Lima and De Ros (2019), Lima *et al.* (2020) and Olivito and Souza (2020), based on high vertical resolution sampling from fewer wells. Despite low vertical representativeness, our samples came from wells widely distributed in the study area though not representing the syn-rift II (SRII) TSS (tectonicstratigraphic

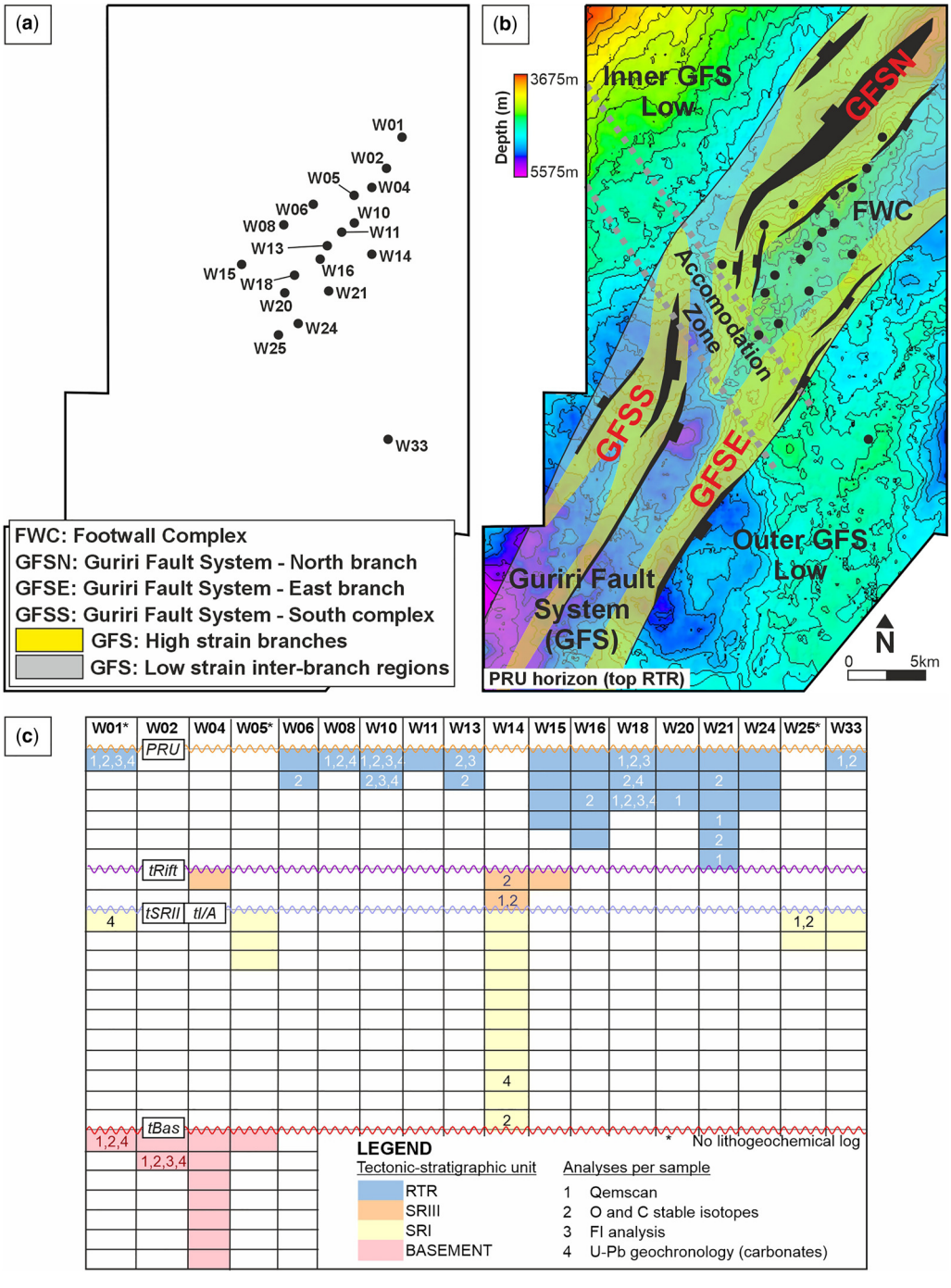

Fig. 2. (**a**) Index map of the wells used in this study. (**b**) Well location overlapped to structural contours of the top of rift transition surface, main structural compartments and simplified fault framework (adapted from Strugale and Cartwright 2022). (**c**) Compilation of the samples used in this study and the respective analyses. Petrography was performed in every sample. Notice that syn-rift phase II (SRII) is not penetrated by any well and is therefore included within SRI tectonicstratigraphic sequences. W01, well number 01 etc.

sequence) (not drilled) and having only a few representatives of the SRIII TSS due to its low thickness onto structural highs (Figs 1b & 2c; see also Strugale and Cartwright 2022).

At least one standard-thickness polished thin-section was extracted from each sample after cleaning using toluene and methanol in a Soxhlet apparatus or an ultrasonic bath in isopropanol. Some thin-sections were stained with Alizarin Red S and potassium ferricyanide to differentiate the carbonate minerals as outlined by Dickson (1965). Thirteen samples were cut and placed in resin pods for automated mineralogical distribution mapping using QEMSCAN (FEI) equipment at Rocktype Ltd laboratory in Oxfordshire (UK).

Mineralogy check using X-ray diffraction (XRD) and stable isotope measurements (oxygen and carbon) were made at the Department of Earth Sciences, University of Oxford (UK). Powder from 20 diagenetic phases, selected from 12 wells, was generated by micro-drilling and analysed on a PANalytical Empyrean Series 2 powder X-ray diffractometer operating at 40 kV and 40 mA with a Co Kα source to establish mineralogy and to check for the presence of carbonates. Four out of 20 were discarded due to low or absent carbonate content. Carbonate powders from the 16 remaining samples were analysed for $\delta^{13}C$ and $\delta^{18}O$ on a Thermo Delta V Advantage isotope ratio mass spectrometer (IRMS) equipment fitted with a Gas Bench II peripheral. Within the Gas Bench II, the powdered samples, in 12 ml He-flushed exetainers (Labco), were reacted with 100% phosphoric acid at 50°C. The relative $^{13}C/^{12}C$ values are reported in the conventional $\delta^{13}C$ (‰) notation, relative to the Vienna Pee Dee Belemnite (VPDB), by assigning a value of +1.95‰ exactly to NBS-19 reference material. The relative $^{18}O/^{16}O$ values are reported in the conventional $\delta^{18}O$ (‰) notation, relative to VPDB, on a normalized scale such that the $\delta^{18}O$ of NBS-19 is −2.2‰. Reproducibility of in-house marble standard NOCZ during these analytical runs was 0.03‰ for $\delta^{13}C$ and 0.07‰ for $\delta^{18}O$ (1σ, $n = 8$), with average $\delta^{13}C = 2.22$‰ and $\delta^{18}O = -1.94$ ‰ within the combined uncertainty of the long-term average of NOCZ ($\delta^{13}C = 2.17 \pm 0.06$‰; $\delta^{18}O = -1.90 \pm 0.09$‰; 1σ; $n = 120$).

Ten thick thin-sections (>100 µm) from six wells were selected to obtain U–Pb ages of carbonates from several paragenetic phases. Initially, the samples were imaged through cathodoluminescence (CL) to support the identification of growth phases that would guide the spots for LA-ICP-MS. The cold cathode cathodoluminescence (CC-CL) analysis was performed using a NewTec Scientific Cathodyne® system installed at the British Geological Survey (BGS; Nottingham, UK). Frame-by-frame images were stitched using the imageJ plug-in and methodology of Preibisch *et al.* (2009). Subsequently, samples were analysed using the LA-ICP-MS U–Pb geochronology procedures of Roberts *et al.* (2017). The analyses were performed in the Geochronology and Tracers facilities at the BGS (Nottingham, UK). A static spot ranging from 60 to 100 µm was used depending on the target size; spot sizes were kept consistent for each session, and between samples and reference materials. All quoted ages are lower intercept $^{206}Pb/^{238}U$ dates from Tera-Wasserburg plots, at 2σ, with propagated systematic uncertainties. Regressions are unanchored as the spread in data permits the accurate assessment of the upper intercept (the initial $^{207}Pb/^{206}Pb$), and goodness of fit is evaluated using the mean square of weighted deviates (MSWD). More details on the quality controls are available in Rochelle-Bates *et al.* (2022).

Fluid inclusions (FI) on pore-filling saddle dolomite, prismatic and macrocrystalline quartz, and blocky and vein-filling calcite, were studied in double-polished rock chips. Microthermometric measurements of individual fluid inclusions were conducted by Pore Scale Solutions Ltd using a Linkam TMSG600 heating and freezing stage attached to a Zeiss Axio Imager microscope. FIs were described using the approach of Roedder (1984), where FIs were classified according to genetic type (primary, secondary and pseudo-secondary) and linked to the paragenetic phase. Groups of genetically related FIs were considered as fluid inclusion assemblages (FIA). The microthermometric analyses followed the general temperature-cycling methodology for the study of FIs in diagenetic cements outlined by Goldstein and Reynolds (1994). Homogenization temperature determinations (T_h) were made before ice-melting determinations. The ice-melting data were used to model salinity for aqueous FIs. The calculation of the salinity of FIs was undertaken by comparing microthermometric data with the phase relations in experimentally determined salt–water–gas systems under equilibrium conditions for the NaCl–H_2O, $CaCl_2$–H_2O and NaCl–H_2O–$CaCl_2$ systems (e.g. Oakes *et al.* 1990). Where paired temperature of final ice melting (T_{ice}) and temperature of hydrate melting (T_{hyd}) were available, the code *CalcicBrine* (Naden 1996) was used to calculate salinities in terms of the NaCl–$CaCl_2$–H_2O system. In the absence of T_{hyd} data, salinities were calculated in terms of the NaCl–H_2O system for $T_{ice} \geq -21.3$°C and by artificially extending the freezing-point suppression curve (NaCl–H_2O) for $T_{ice} < -21.3$°C.

Results

This section aims to present the detailed investigations performed on the studied samples, from petrography and geochemistry to geochronology (Fig. 2b).

Initially, samples were described as either host rock or diagenetic facies. In the latter, the original lithology and texture are unrecognized due to the intensity of diagenesis. From that starting point, focus shifted to diagenetic products (cements, vugs, fractures and veins), which were investigated using QEMSCAN, stable isotopes, FI microthermometry and U–Pb geochronology. These data allowed the characterization of the diagenetic events and their environments, and the correlation of them with the tectonic and magmatic events of the Campos Basin.

Petrography

The rocks described through petrography were initially classified into five lithofacies (crystalline basement, bioclastic grainstones and rudstones, hybrid arenites and siltstones, arkoses and conglomerates). These lithofacies will be briefly discussed in 'Host rocks' below, since our focus is on the diagenetic products. Because the SRI conglomerates and arkoses have not been described in the previous works in the north of the Campos Basin, a brief petrographic description is provided. Otherwise, the reader is referred to previous publications on the crystalline basement (Strugale *et al.* 2021) and on the RTR and PR sequences (Herlinger *et al.* 2017; Lima and De Ros 2019; Lima *et al.* 2020; Olivito and Souza 2020). Three diagenetic-related facies (dolostones, cherts and breccias) were recognized and described, which often include tectonic and compaction-related features, such as fractures, veins and stylolites. Mosaics of the thin-sections and further QEMSCAN imagery are provided as supplementary material to provide a context for the textures that could not be seen from thin-section snapshots, and the complex distribution of the minerals.

Host rocks

Crystalline basement: These samples are granites with variable quantities of phyllosilicates. Two out of 11 basement samples from wells 01 and 02 (W01 and W02) exhibit widespread brecciation and a discrete vein network, respectively. These fractures are filled by quartz, pyrite and dolomite–ankerite (Figs 3a & 4b). The brittle deformation in these samples could be related to their proximity to the northern branch of the GFS (GFSN branch; Fig. 2b).

Conglomerates and arkoses: These are constituted of lithic conglomerates and arkoses with fine to granule-size grains, representing the SRI sequence (Fig. 1b). There are also conglomerates related to footwall erosion related to syn-rift III (SRIII), but they are indistinct within the samples analysed (Strugale and Cartwright 2022). The lithic grains are made of basement and basalt with dimensions up to pebble size. In the conglomerates, the clasts are commonly covered by oxide rim (probably hematite; Fig. 3b). In the arkoses, clasts are dominated by equal proportions of feldspars (mostly K-feldspars) and quartz, followed by detrital muscovite, lithic grains and zircon; the grains are mostly angular and the rocks are poorly sorted (Fig. 3c). The cement is carbonatic and constituted of Fe-dolomite to ankerite, which often replaces feldspar grains, leading to an abundance of up to one-third of the sample. Feldspar replacement by Al-phyllosilicates is also common. QEMSCAN data, however, suggests that ankerite replaces the feldspar grains and Fe-dolomite to ankerite constitutes the cement (see inset on Fig. 3c). The constitution and paragenetic phases of SRI are similar to observations made in the equivalent section in the Central Campos Basin (Carvalho and De Ros 2015).

Conglomerates occur in all the wells that penetrated the SRI sequence, but coarser and compositionally more heterogeneous specimens occur in W05, located along the trace of the GFSN branch (Fig. 2). The occurrence of conglomerates with basement and basalt clasts is related to significant footwall uplift and erosion during the SRII and SRIII sequences (Strugale and Cartwright 2022) (Fig. 1b). Samples from W14, W25 and W33, located away from the GFS branches, tend to have a more homogeneous composition and well-sorted character with minor lithic fragments (Fig. 2b).

Bioclastic rudstones and grainstones: The bioclasts are commonly constituted of disaggregated bivalves and ooids replaced by micrite, fine-grained blocky dolomite and chalcedony (Fig. 3d). The cement could be either blocky to prismatic quartz or blocky calcite. Extensive vug-related porosity could occur in the intragrain space when it is not partially or completely obliterated by macrocrystalline calcite (Fig. 5a). Vugular porosity is common, but many of the analysed samples are completely recrystallized by calcite, quartz and minor dolomite (Figs 6a & 7b, respectively). Veins are predominantly filled by calcite, sometimes with fracture walls lined with prismatic quartz. One vein in a bioclastic rudstone has a distinct suite of minerals constituted of massive pyrite with minor nuclei of chalcopyrite and nearby vugs partially filled by Sr-barite (Fig. 4e).

The occurrence of bioclastic rudstones and grainstones in the SRIII + RTR with moderate to high shell reworking is interpreted as a predominantly shallow lacustrine depositional environment, influenced by longshore and storm currents (Olivito and Souza 2020). These authors also observed an overall coarsening-up and shallowing-up sequence from SRIII to RTR sequences. The wells located in the hanging wall of the GFSN branch (W06, W08 and W15) also have the occurrence of high-energy lithofacies as RTR prograding mounds onto low-energy deposits (Strugale and Cartwright 2022). These low-

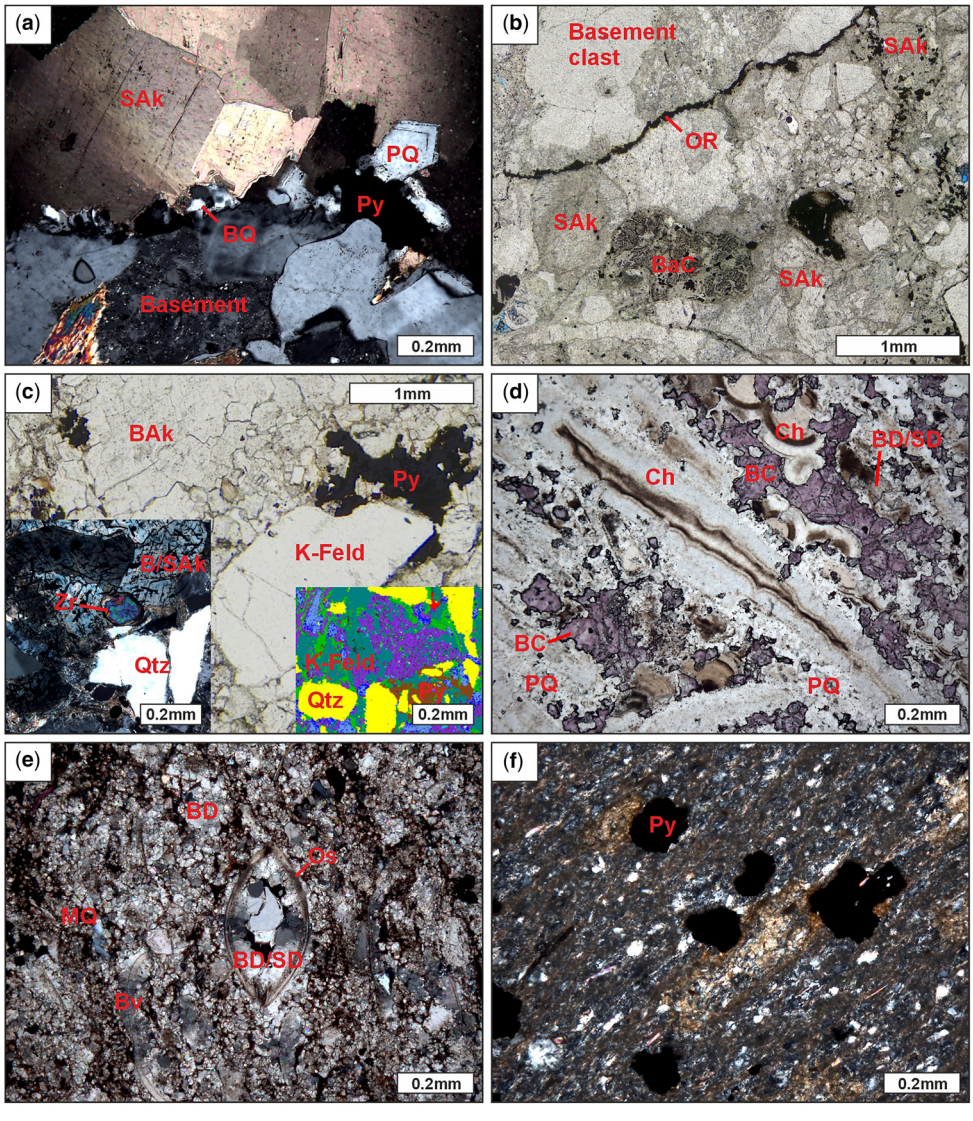

Fig. 3. (**a**) Brecciated Precambrian basement with post-deformational overgrowth of pyrite (Py), blocky quartz (BQ), prismatic quartz (PQ) and saddle ankerite (SAk) onto a clast of basement (BC) (XPL). (**b**) Lithic conglomerate constituted of clasts of basement and basalt clasts (BaC) cemented with saddle ankerite (SAk). Notice the oxide rim (OR) around some of the clasts (PPL). (**c**) Very coarse arkose with K-feldspar (K-Feld) clasts and cement made of pyrite (Py), blocky ankerite (BAk) and saddle ankerite (SAk) (PPL). Qtz, detrital quartz. The small insets show the blue-stained Fe-dolomite cement and zircon grain (Zr) (left) and QEMSCAN imagery showing K-Feld partially replaced by ankerite (purple), Al-phyllosilicates (light green) and ankerite/Fe-dolomite (blue) cement. (**d**) Rudstone made of fragmented bivalve bioclasts replaced by blocky dolomite (BD) with intraparticle space with botryoidal chalcedony (Ch) and blocky calcite (BC) (PPL). (**e**) Bioclastic arenite with ostracod (Os) and fragmented bivalves (Bv) in a matrix of blocky dolomite (BD), saddle dolomite (SD), microcrystalline quartz (MQ) and Mg-clay (XPL). (**f**) Siltstone with detrital quartz and white mica in Mg-clay matrix and post compaction pyrite nodules (Py) (XPL).

energy facies constitute the next group of samples to be described.

Hybrid arenites and siltstones: These occur in the seven wells and indistinctly in SRI–SRIII sequences. They are characterized by variable proportions of clastic and bioclastic constituents in a notable proportion of magnesian clay (mostly stevensite; see Herlinger *et al.* 2017) or organic

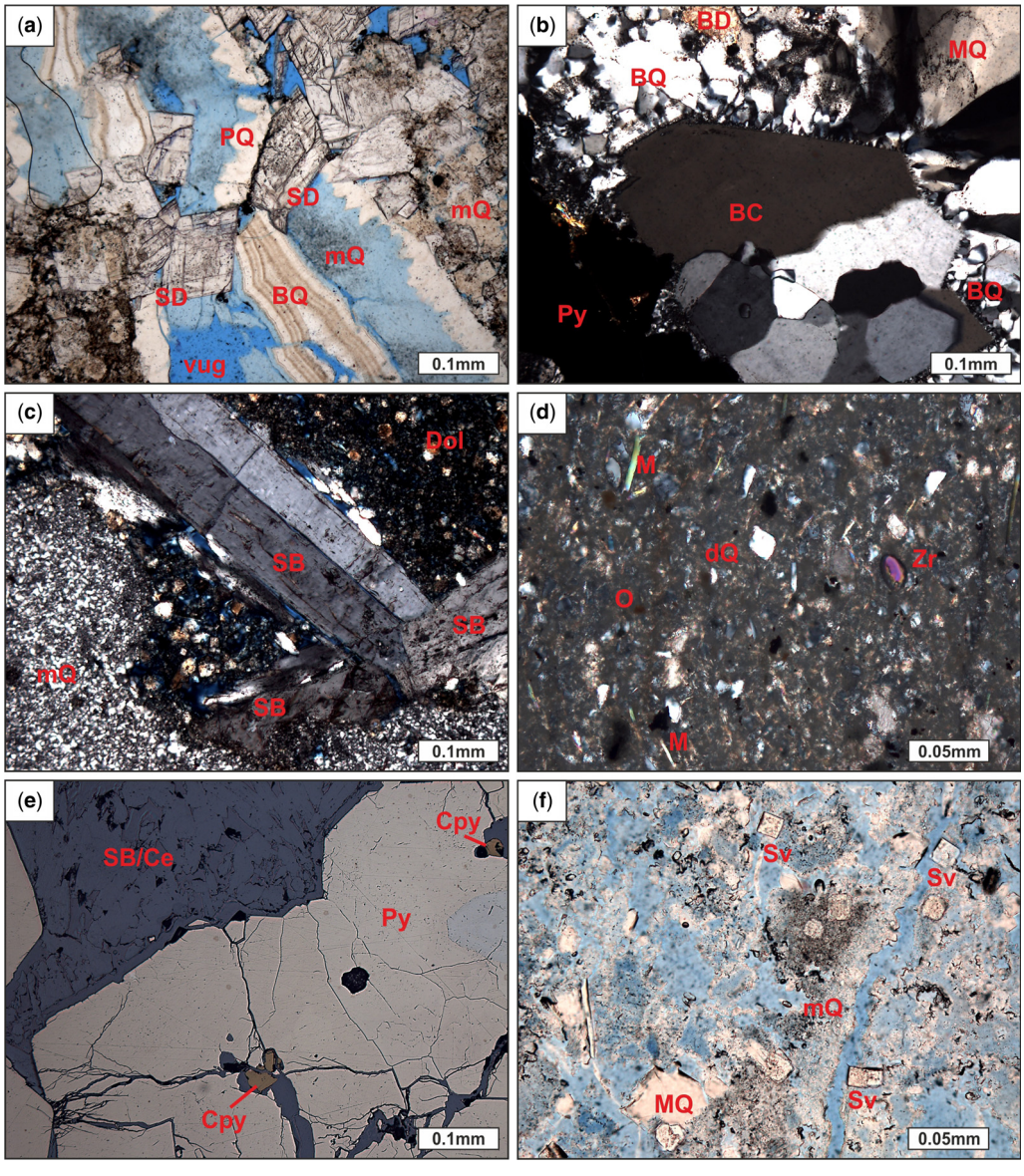

Fig. 4. Aspects of diagenetic products and accessory detrital and diagenetic minerals. (**a**) Breccia constituted of a microcrystalline quartz as matrix with saddle dolomite (SD), botryoidal quartz (BQ), prismatic quartz (PQ), late porous microcrystalline quartz (mQ) and open vugs (PPL). (**b**) Shear fracture filled with pyrite (Py). The damage zone is constituted of basement clast (BC) with prismatic quartz (PQ) and macrocrystalline quartz (MQ) onto it (XPL). (**c**) Microcrystalline quartz (mQ) matrix and a vug filled with prismatic Sr-barite (SB) and dolomite (Dol) (XPL). (**d**) Siltstone with abundant organic matter (O) on which is observed detrital quartz (dQ), mica (M) and zircon (Zr) (XPL). (**e**) Sulfide vein constituted of macrocrystalline pyrite (Py), some chalcopyrite (Cpy) and Sr-barite to celestine (SB/Ce) (RL). (**f**) Svanbergite cubes (Sv) in a matrix of partially dissolved microcrystalline quartz (mQ) and some macrocrystalline quartz (MQ) (PPL).

matter in the matrix. They are composed of detrital quartz and white mica of coarse silt to fine sand grain size, peloids, disarticulated bivalve shells and ostracods (Fig. 3e); zircon is a common detrital accessory (Fig. 4d). The samples are sometimes completely replaced by dolomite as rhombs and aggregates (Figs 5e & 8a, d), microcrystalline quartz (chert), and blocky chalcedony as nodules

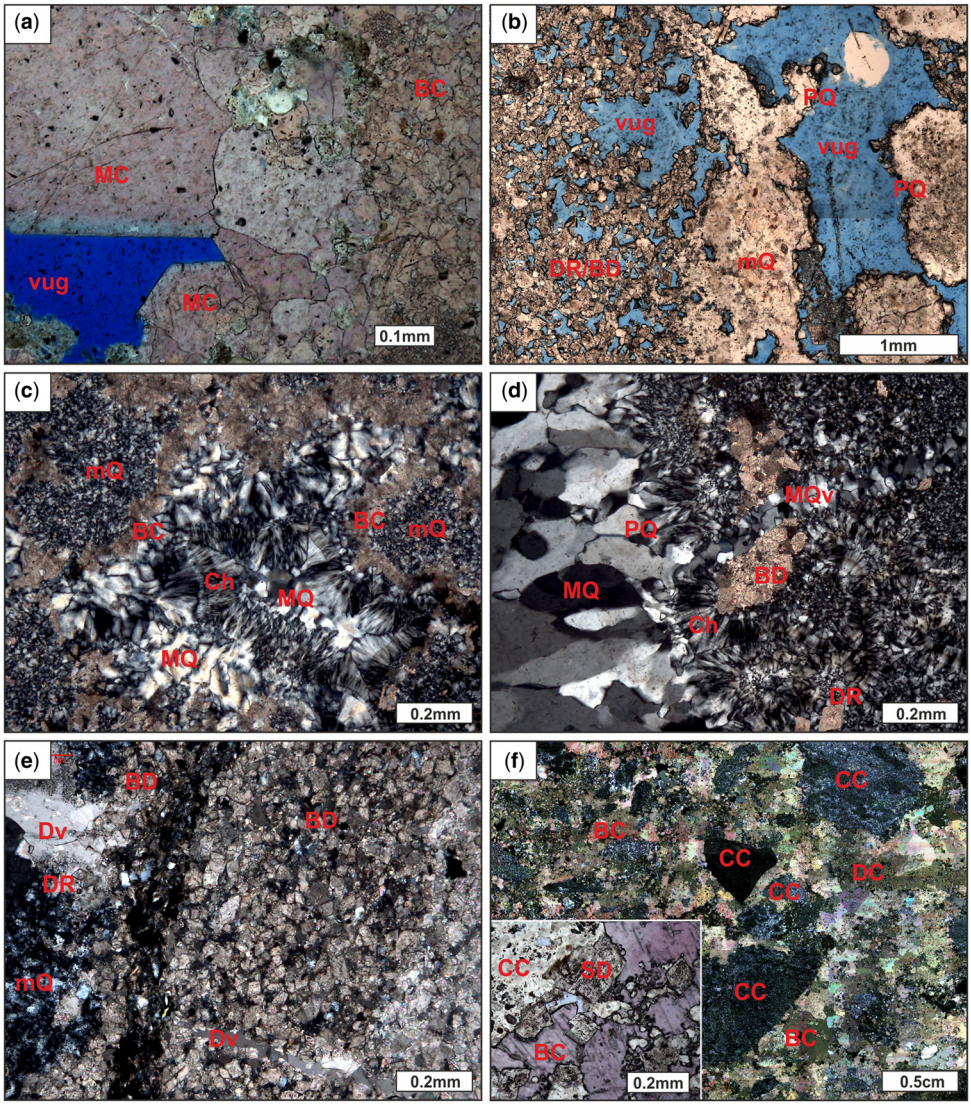

Fig. 5. Silica and carbonatic diagenetic products. (**a**) Ooids and peloids replaced by blocky calcite and vug partially filled with macrocrystalline calcite (MC) (PPL). BC, blocky calcite. (**b**) Extensive vugular porosity in the interface zone between dolostone (left) made of euhedral and blocky dolomite (DR/BD), and chert made of microcrystalline quartz (mQ) and blocky quartz (BC). Vugs in chert have minor Sr-barite crystals (PPL). (**c**) Succession of diagenetic products made of microcrystalline quartz (mQ), blocky calcite (BC), blocky chalcedony (Ch) and macrocrystalline quartz (MQ) (XPL). (**d**) Succession of diagenetic products where early blocky dolomite (BD) is followed by microcrystalline quartz (mQ) and chalcedony (Ch), and finally by quartz as veins (MQv) and vug-filling megacrystals (MQ) (XPL). DR, dolomite rhombs. (**e**) Two generations of dolomite cementation. Extensive early blocky dolomite cement (BD) on the right, with subsidiary dolomite rhombs (DR) in a layer with silica-rich matrix (mQ) on the left, both superimposed by late veins of hyaline dolomite (Dv) (XPL). (**f**) Breccia constituted of chert clasts (CC) and dolostone clasts (DC) in a matrix intensively cemented by hyaline blocky calcite (BC) and saddle dolomite (SD) (XPL). The inset shows the respective stained colours.

and layers (Fig. 8b). Pyrite is also abundant and occurs as either post-compaction dendritic nodules or subvertical veins that are cross-cut by partially filled stratabound fractures (Fig. 3f). Hyaline dolomite veins occur as fracture fill in chert layers and as vug fill in chert nodules, suggesting that

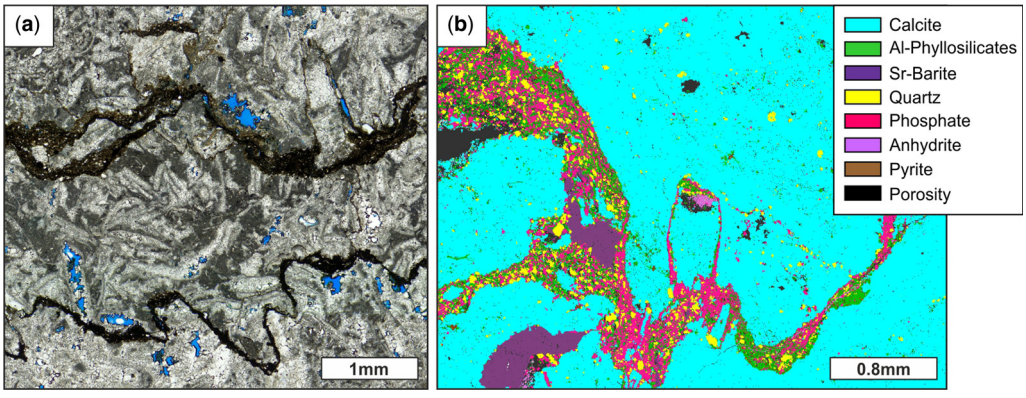

Fig. 6. Two images of the stylolites observed in a sample of bioclastic rudstone intensively cemented by calcite. (**a**) PPL photomosaic showing two systems of stylolites that cross-cut most of the recrystallized matrix constituents. Notice that minor stylolites are cross-cut by major stylolites. (**b**) High-resolution QEMSCAN imagery showing the main mineral constituents of the stylolitic levels. Notice the late vug-fill by Sr-barite and anhydrite.

chert may be more brittle than the dolostones (Fig. 8b, d).

Diagenetic products

Dolostones: These are predominantly made up of dolomite rhombs and aggregates of blocky dolomite in a matrix of Mg-clays, organic matter and detrital clasts (Fig. 8a); in some cases, dolomite crystals represent nearly 100% of the sample (see discussion in (Warren 2000). Dolostones commonly occur interlaminated with or hosting chert nodules (Fig. 5d, e & 8b). Dolomite rhombs, aggregates and saddle dolomite are also common diagenetic products in bioclastic grain and rudstones, although not particularly abundant in these facies and often preceding calcite cements (Fig. 3d).

Saddle dolomite has been associated solely with hydrothermal diagenesis since it often occurs as the latest phase of vug filling and reveals high formation temperatures (Lima *et al.* 2020), while blocky dolomite and dolostones have been interpreted as an eo/mesodiagenetic product of Mg-clay rich lithologies (Lima and De Ros 2019). However, some low-energy deposits have minor dolomite (Fig. 3f), and dolomite rhombs are sometimes engulfed by saddle dolomite, calcite cements and calcite veins, suggesting a temporal series (Fig. 5e, f). In addition, dolomite rhombs apparently precede silica cementation (Fig. 5d). Thus, dolomitization is interpreted as one of the earliest diagenetic phases.

Cherts: This term describes samples or strata that consist mainly of siliceous cement, which frequently masks the original rock and replaces the protolith as microcrystalline, prismatic quartz and macrocrystalline quartz, and chalcedony. Chert cement or entire samples constituting it are widely distributed throughout the SRIII and RTR sequences. Chalcedony and microcrystalline quartz aggregates commonly exhibit halos of immiscible material, thus configuring botryoidal textures (Figs 3d & 4a). Fracturing and dissolution occur in quartz cements and result in networks of interconnected fractures and vugs with significant secondary porosity. Vugs and fractures are commonly filled with minerals such as svanbergite, Sr-barite, calcite and blocky dolomite (Fig. 4c, f & 8f).

The occurrence of chert interlaminated with dolostone probably relates to the primary sedimentary layering, since dolostones reflect a higher abundance of Mg-clay minerals in the host rock and thus lower depositional energy. Therefore, cherts formed in less argillaceous facies, although the common presence of floating dolomite rhombs in cherts suggests that some clays were present. However, such an interpretation could be problematic because the mechanisms that govern the coexistence of siliceous cement and dolomitization are not well understood (Hesse 1989; Packard *et al.* 2001; Bustillo 2010). Also, it is often impossible to identify the protolith of cherts and thus assess its primary porosity, making any assumption on the original clay content and primary porosity problematic. On the other hand, dolomitization of Mg-clays releases orthosilicic acid, which could explain the common occurrence of siliceous cements in dolostones (Lima and De Ros 2019). Hybrid lithologies contain detrital quartz that could also provide diagenetic silica. However, extensive quartz precipitation in fractured basement suggests that it may constitute an external source of silica (Fig. 4b). Hence, the abundance of silica cement across the sedimentary section suggests the presence of an external source of silica that could either be represented by the crystalline basement or by the SRI arkoses.

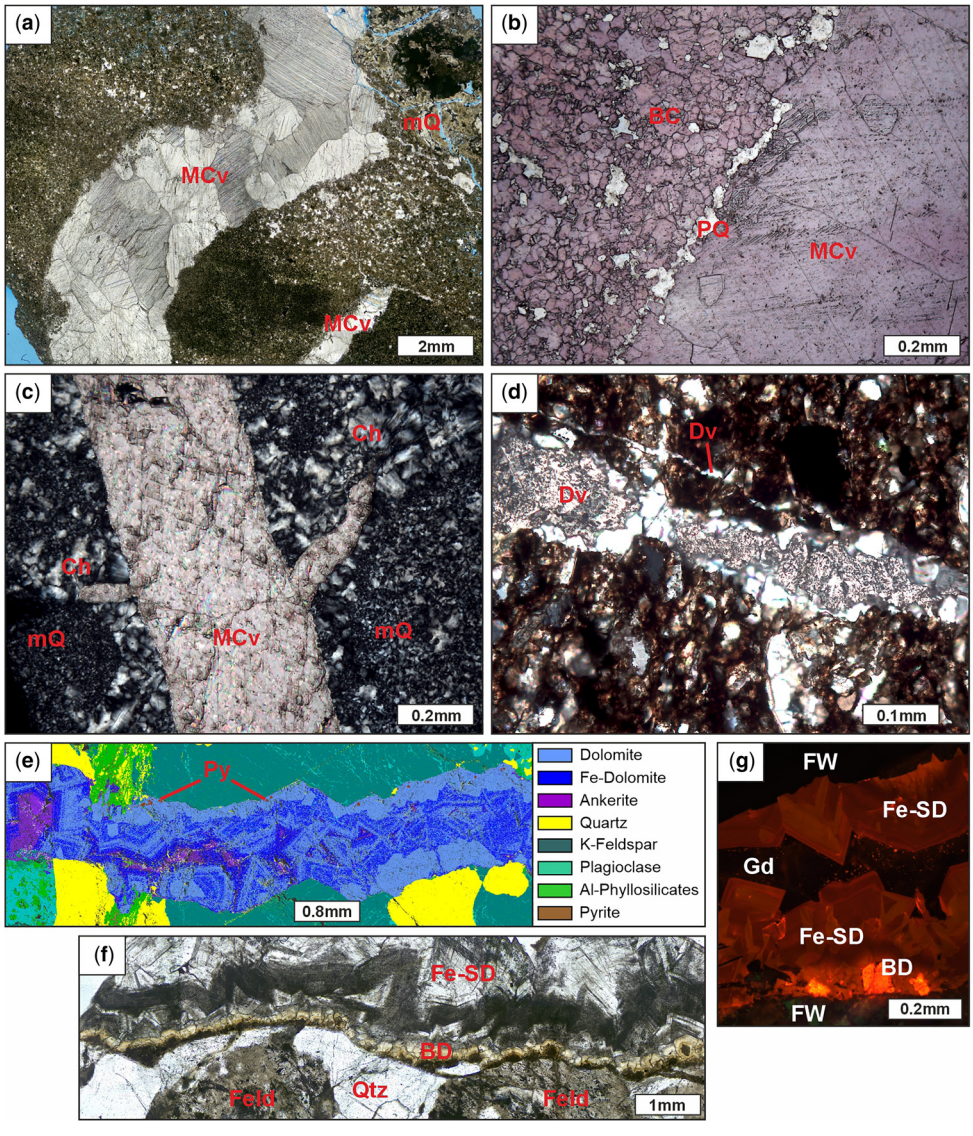

Fig. 7. Comparison between calcite and dolomite veins. (**a**) Veins of macrocrystalline calcite (MCv) in dolostone with some microcrystalline quartz (mQ) cement (PPL). (**b**) Vein constituted of macrocrystalline calcite (MCv) with a rind of prismatic quartz (PQ) onto a host rock of bioclastic rudstone cemented by blocky calcite (BC) (PPL, stained). (**c**) Sub-vertical macrocrystalline calcite-filled vein (MCv) with subsidiary veins at right angle in a host rock constituted of microcrystalline quartz (mQ) and chalcedony (Ch) (XPL). (**d**) System of sub-vertical dolomite-filled veins (Dv) in a layered hybrid siltstone (XPL). (**e**) High-resolution QEMSCAN imagery and (**f**) photomosaic of a crack-vein in basement (Feld, feldspar; Qtz, quartz sample filled by a sequence of blocky dolomite (BD) with pyrite (Py) nodules, saddle Fe-dolomite (Fe-SD) and ankerite (PPL). Notice in 'e' the compositional gradation/zonation from dolomite, Fe-dolomite than ankerite towards the centre of the vein. (**g**) Cathodoluminescence (CL) image of the fracture of (e) and (f) showing bright red-orange colour for the blocky dolomite (BD), pale orange colour with well-developed growth rims (Fe-SD) and dull brown with speckled orange in the later ankerite gap deposit (Gd) in the centre. FW: fracture wall.

Breccias: These were identified in samples from both the basement and sedimentary sections and are solely composed of intraclasts, which makes them distinct from the conglomerates. Two types of breccia occur, clast-supported *in situ* breccias (cracking breccia) and matrix-supported breccias.

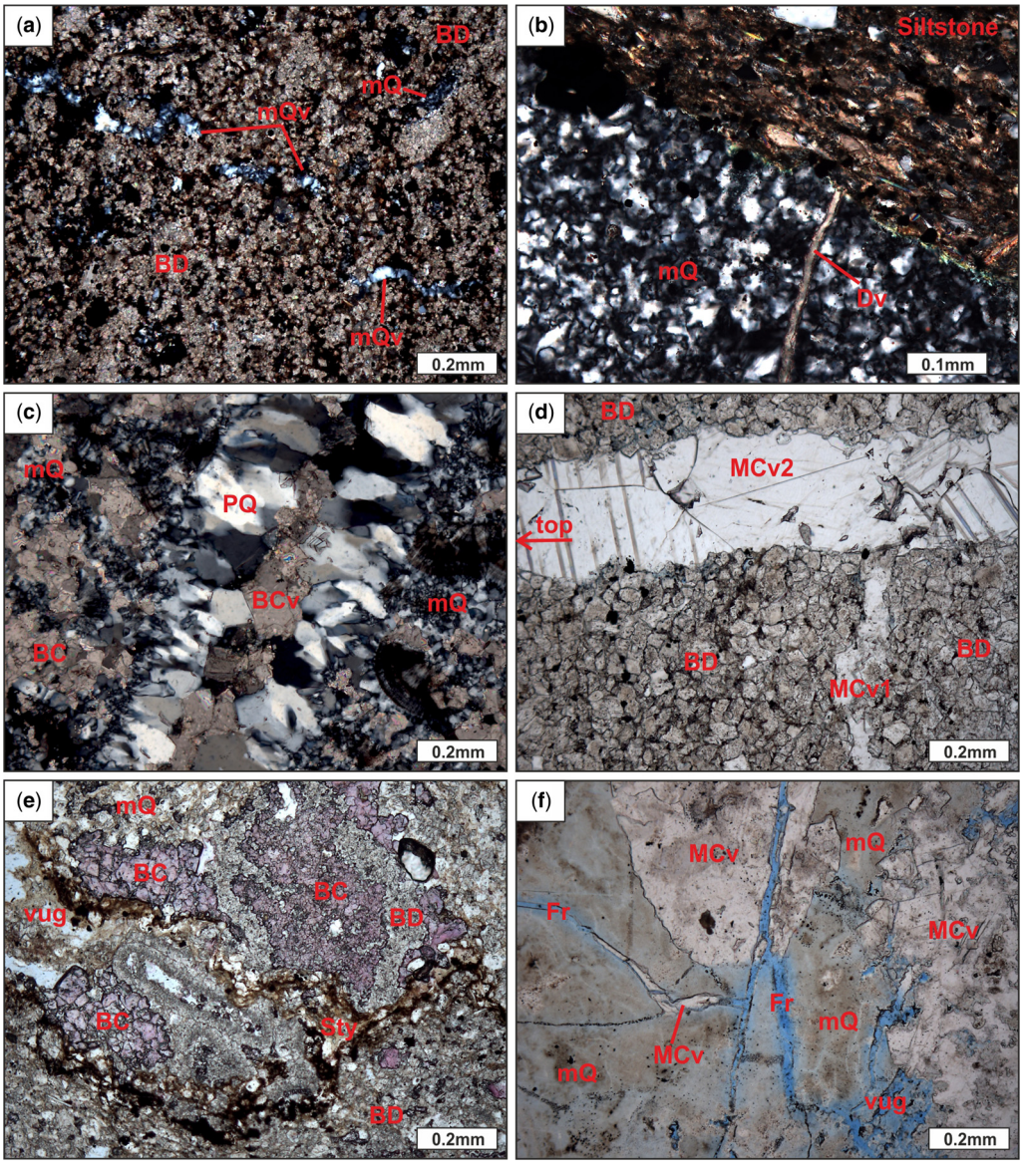

Fig. 8. Tectonic and compaction features. (**a**) Ptygmatic folding in microcrystalline quartz (mQv) veins in a matrix of blocky dolomite (BD) and microcrystalline quartz cement (mQ) (XPL). (**b**) Contact of dolomitized siltstone and a layer of microcrystalline quartz (mQ) with a dolomite vein (Dv) (XPL). (**c**) Vein initially filled with lined prismatic quartz (PQ) and later blocky calcite (BCv). The matrix is made of replacive blocky calcite (BC) and microcrystalline quartz (mQ) cement (XPL). (**d**) Dolostone with replacive calcite cement showing an early bed-parallel calcite vein (MCv1) crossed by a vertical macrocrystalline calcite vein (MCv2) (PPL). (**e**) Stained section showing stylolites (Sty) associated to vugular porosity in a matrix made of peloids replaced by blocky calcite (BC) and blocky dolomite (BD) (PPL). (**f**) Chert (mQ) showing multiple events of fracturing, brecciation, dissolution and selective filling of macrocrystalline calcite (MCv) (PPL). Fr, fracture.

Breccias occur relatively close (<50 m in depth) to unconformities, where samples from W01 and W15 are next to tRift unconformity, and the W18 sample is close to PRU (Fig. 2c).

Breccias in basement rocks are exemplified in Figure 4b, on which a shear fracture exhibits extensive brecciation, resembling a fault plus damage-zone system. This breccia is filled with pyrite, quartz

and saddle Fe-dolomite. Within the sedimentary succession, several samples show some degree of fracturing that has locally generated brecciated textures (Figs 4e & 8f) but are best exemplified in Figure 5f. These are dilatational, cement-supported breccias comprising up to 1 cm angular clasts of microcrystalline quartz and subsidiary dolostone clasts; both occur in the matrix as finer fractions. Earlier cement is constituted of blocky and saddle dolomites, followed by pervasive blocky to macrocrystalline calcite cement.

The breccia of Figure 5f is interpreted to have formed at some depth since both chert and dolostone clasts were lithified prior to brecciation, to form a hydrothermal-related breccia that was later cemented by calcite. Breccias are a common product of hydrothermal diagenesis in the context of hypogenic karstification and occur along faults and below low-permeability strata (e.g. Davies and Smith 2006; Kyne *et al.* 2019). However, the possibility of this breccia being surficial and related to epigenetic karst is not excluded, since it is relatively close to the PRU unconformity. Matrix-supported breccias are also a common product of epigenetic karst (Loucks 1999).

Tectonic, compaction and dissolution features

Tectonic and compaction features are represented by veins filled with carbonates, quartz and occasionally sulfides; stylolites, open fractures partially filled with calcite or dolomite, and folded sand dykes also occur. Veins and fractures are either bedding-parallel or orthogonal with respect to the sedimentary layering. Brecciated texture is commonly associated with fracture sets, especially in cherts.

It was impossible to determine the direction of veins in unstratified rocks, such as basalt and basement. Their walls are straight and sharp in more cohesive rocks (basement, basalts and cherts) and wavy to irregular in porous ones (arkoses, rudstones and dolostones).

In the bioclastic grain and rudstones of SRIII + RTR sequences, calcite is the predominant vein-filling mineral, followed by quartz (e.g. Fig. 7b). Notice that within these lithologies the vein composition resembles that of the fracture wall (Figs 6b & 7b). On the other hand, dolomite is the principal vein-fill in dolostones, hybrid siltstones and arenites (Fig. 7d).Veins in basement and basalt are filled by dolomite to ankerite series, including Fe-dolomites that are either lining the fracture walls (Fig. 7e–g) or disseminated within the cataclastic matrix (Figs 3a & 4b). In the first example, the transition from rims of blocky dolomite with pyrite nodules to ankerite is evident. Following partial dissolution of the blocky dolomite, saddle Fe-dolomite with well-defined growth rims formed, followed by gap deposits (cf. Laubach *et al.* 2019) constituted by ankerite exhibiting speckled CL. In the second case, cataclastic-related cements are made of speckled saddle Fe-dolomite and saddle ankerite which are associated with early pyrite and rims of prismatic quartz to blocky quartz (Fig. 3a).

In bioclastic grainstones and rudstones, as well as cherts and some dolostones of SRIII + RTR, veins of macrocrystalline calcite predominate and are chemically homogeneous according to QEMSCAN images (Fig. 7a–c). Other minerals that occur within calcite veins are dolomite, as floating rhombs, and rims of blocky and prismatic quartz that precede calcite precipitation (Figs 7b & 8c). An exception is the vein or vug in bioclastic rudstone shown in Figure 4e. This vein is mainly filled by non-replacive pyrite nodules, some of which exhibit nuclei of chalcopyrite and sphalerite; pyrite is increasingly fractured towards the margins. These fractures were filled with fibro-radial Sr-barite and anhydrite, which also fills open vugs in nearby host rock, similarly to that observed in Figure 6b. Although pyrite is a common diagenetic product in clay-rich rocks – because of thermochemical sulfate reduction of organic matter and the formation of pyrite nodules (Machel 2001) – its occurrence as fracture-fills in either basement or SRIII rudstones, and in Fe-rich dolomites, suggests remobilization during diagenesis.

Quartz veins are less common and are typically related to quartz-rich lithologies (Figs 5d & 8c). Due to the difficulty of recognizing sedimentary layering in samples with intense quartz cementation, it was not possible to recognize a preferred orientation. One exception is a subvertical, folded quartz vein in dolostone which suggests the mechanical compaction of a sand dyke during burial and its eodiagenetic emplacement (Fig. 8a). In Mg-clay-rich lithologies, dolomite veins were identified crossing chert layers interlaminated with siltstones (Fig. 8b).

Stylolites were observed in bioclastic rudstones, hybrid lithofacies and cherts, despite the abundance of clay minerals in the host rock (Fig. 6a). Petrography and QEMSCAN mapping show that stylolites are characterized by high concentrations of clay minerals (mostly illite), pyrite, barite, anatase (rutile), phosphate, anhydrite and quartz grains that were involved during the stylolite development (Fig. 6b). Contact relationships between bioclasts, cements and stylolites show truncations which suggest multiple events of dissolution and mineral concentration by pressure solution. Well-developed stylolites cross-cut the thinner ones and most of the cement phases. On the other hand, stylolites in interlaminated hybrid facies tend to occur in the contact zone between chert and dolostone. When occurring in bioclastic rudstones and cherts,

stylolites are often accompanied by symmetric porosity enhancement, similar to observations in the Maestrat Basin, Spain (Martín-Martín *et al.* 2018).

QEMSCAN bulk composition

The bulk compositions of the samples analysed by QEMSCAN (QS50 and QS4) provide the proportions of major and some minor elements. Examples of QS4 images are shown in Figures 3c, 6b and 7e. Table 1 reveals quartz and calcite as the most abundant minerals in the carbonate phases, followed by the dolomite group (dolomite to ankerite) and accessory minerals in the form of Al-phyllosilicates, anatase (rutile), phosphates, pyrite and barite/celestine. The proportions of K-feldspar and plagioclase are similar, and quartz predominates in the basement, which is granodioritic in composition. The arkose of W25 has a prevalence of K-feldspar and quartz over plagioclase, which could be related to the diagenetic replacement of the latter by ankerite (Fig. 3c). Overall porosities range from 0.56 to 16.02% and show no correlation with any mineral constituent.

Stable isotopes

The range of $\delta^{13}C$ values is mostly concentrated in an interval between −1.68‰ and 1.66‰, with a mean value of 0.85‰ (Table 2, Fig. 9). These results are similar to those described for diagenetic phases in these rift sediments by Lima *et al.* (2020), even though samples from the present study are largely from rift units that were not sampled by the latter study. This observation is also valid for mineral phases like Fe-dolomite cement in arkoses and calcite cement in *in situ* breccia. The observed ranges for $\delta^{13}C$ are compatible with either marine-water or freshwater carbonates (Hoefs 1997) and do not reflect forced hydrocarbon maturation by hydrothermal diagenesis, as observed in the counterpart Namibe Basin in Africa (Rochelle-Bates *et al.* 2021). There is no correlation between $\delta^{13}C$ and $\delta^{18}O$ values, which is also a feature of previous studies in the Campos, Santos and Kwanza basins (Ceraldi and Green 2017; Farias *et al.* 2019; Lima *et al.* 2020; Pietzsch *et al.* 2020).

In contrast to the restricted $\delta^{13}C$ values, $\delta^{18}O$ values from the analysed carbonates show a wider variation (from −0.72‰ to −9.65 ‰ – Fig. 9). It is observed that coarser, vein-filling calcite and dolomite have lower $\delta^{18}O$ than the pore-filling carbonate cements and the replacive carbonates. For example, in Figure 7b the blocky calcite cement in the matrix and the macrocystalline calcite vein-fill have $\delta^{18}O$ values of −3.57‰ and −8.79‰, respectively. This decrease to lower $\delta^{18}O$ towards the youngest mineral phases suggests either differences in the temperature of the fluid and/or in the oxygen isotopic composition of the vein fluid ($\delta^{18}O_w$). Therefore, the progressive decrease in $\delta^{18}O$ over time is interpreted to reflect repeated recycling events (dissolution and precipitation) causing lower $\delta^{18}O$ in later cements. In other words, veins are the latest diagenetic phase and yield the lowest $\delta^{18}O$ values (*c.* −8.79‰) because the host rock provides oxygen isotopes with lower $\delta^{18}O$ (−3.57‰). These, in turn, are lower than the earliest microcrystalline calcite (*c.* −1.00‰, Fig. 9). Despite the analysed samples being representative of the most diagenetically altered lithofacies, our $\delta^{18}O$ results still fit within the ranges of both syngenetic and hydrothermal phases in the Campos Basin (Lima *et al.* 2020).

Fluid inclusions

Over 360 liquid plus vapour (L + V) FIs were analysed in 7 rock wafers representing the major mineral phases (quartz, calcite and dolomite) to detect spatial variations in the homogenization temperature (T_h) and salinity. Figure 10 presents a graphic summary of T_h and salinity (wt% NaCl eq.) determinations for the mineral phases investigated. The complete dataset is shown in Table 3 and the detailed description are presented as supplementary material.

The majority of FIs are primary and aqueous. Numerous FIs are defined as pseudosecondary since they could not be categorized as either primary or secondary. Considering such uncertainty, we opt to disregard the morphology of the FIs and classify them as primary or pseudosecondary. Only a few hydrocarbon-bearing FIs were described, and these do not contain a resolvable aqueous phase.

T_h average at 106.1°C (median of 105°C) and increase with depth (Fig. 10c). T_h in calcites show unimodal distributions with peaks around 95 and 105°C, respectively; macrocrystalline quartz shows two major quartiles, at 100–105 and 120–125°C. While the overall T_h range of the dolomite phases is similar to that of calcite and quartz, they have more dispersed distributions and do not exhibit any pattern. Despite the similarity of values from the present study with those of Lima *et al.* (2020), the wide range of T_h observed is nevertheless interpreting as reflecting variable fluid temperature during the diagenesis.

The salinities are generally high for all mineral phases except saddle dolomite (Fig. 10b). The average and median salinities are 21.9 and 22.8 wt% NaCl eq., respectively. Blocky calcite and macrocrystalline calcite veins have contrasting distributions, right- and left-skewed, respectively. Therefore, blocky calcite has the highest average and median values for salinity (22.7 and 23.7 wt% NaCl eq., respectively).

Table 1. Bulk composition of the samples analysed by QEMSCAN at 50 μm resolution

Depth (m)	Well	TSS	Calcite	Dolomite	Fe-Dolomite	Ankerite	Quartz	K-Feldspar	Plagioclase	Al-phyllosilicates/ Illite/Smectite	Anatase	Phosphate	Pyrite	Barite	Anhydrite	Chalcopyrite	Sphalerite	OtherPhases	Porosity
XX58.5	W01	RTR	0.2	10.7	0.7	0.0	78.3	0.0	0.0	1.8	0.0	0.1	0.2	0.0	0.0	0.0	0.0	0.2	7.7
XX90	W01	BAS	0.1	2.6	1.1	0.4	29.8	25.5	31.1	7.0	0.0	0.1	0.0	0.0	0.0	0.0	0.0	0.1	2.2
XX93	W02	BAS	0.1	0.9	2.4	10.7	33.8	17.8	16.0	7.2	0.1	0.1	5.4	0.0	0.0	0.0	0.0	0.3	5.0
XX60	W08	RTR	1.8	55.0	1.5	0.0	25.3	0.0	0.0	0.0	0.0	0.1	0.0	0.0	0.0	0.0	0.0	0.1	16.0
XX11	W10	RTR	90.2	0.0	0.0	0.0	1.5	0.0	0.0	1.0	0.0	1.4	0.2	0.1	0.0	0.0	0.0	0.0	5.5
XX80	W14	SRIII	54.8	0.0	0.0	0.0	24.1	0.0	0.0	0.0	0.0	0.0	9.7	2.2	0.6	0.0	0.0	0.1	8.3
XX42.2	W18	RTR	29.5	9.0	1.2	0.0	48.2	0.0	0.0	0.9	0.0	0.3	0.0	0.0	0.0	0.0	0.0	0.1	10.9
XX48.5	W18	RTR	33.8	0.6	0.1	0.0	62.2	0.0	0.0	0.2	0.0	0.0	0.0	0.0	0.0	0.0	0.0	0.0	3.0
XX75	W20	RTR	22.0	0.9	0.0	0.0	75.7	0.0	0.0	0.4	0.0	0.1	0.0	0.0	0.0	0.0	0.0	0.0	0.8
XX40	W21	RTR	2.5	19.0	1.0	0.0	46.1	0.3	0.0	17.8	0.2	4.0	1.1	0.0	0.3	0.0	0.0	0.3	7.5
XX48	W21	RTR	4.0	0.0	0.0	0.0	90.6	0.0	0.0	0.0	0.0	0.0	0.0	0.1	0.0	0.0	0.0	0.0	5.2
XX75	W25	SRI	0.3	8.6	4.1	9.0	21.0	27.2	0.2	22.7	0.6	0.3	1.1	0.0	0.0	0.0	0.0	0.4	4.4
XX08	W33	RTR	84.6	0.0	0.0	0.0	0.3	0.0	0.0	0.0	0.0	0.3	0.0	0.0	0.0	0.0	0.0	0.0	14.6

BAS, crystalline basement; RTR, rift transition; SRI and SRIII, syn-rift phases I and III, respectively; TSS, tectonostratigraphic sequence (Fig. 1b).

Table 2. Stable isotope $\delta^{13}C$ and $\delta^{18}O$ from several lithofacies, including with distinct diagenetic cements

TSS	Mineral phase	Well	Depth (m)	XRD mineralogy	$\delta^{13}C$	s.d.	$\delta^{18}O$	s.d.	Sampling observation
Basement	SD	W01	XX90	DOL 98%, CAL 2%	−1.68	0.03	−9.65	0.03	Manual picking of vein-filling saddle dolomite
RTR	BD/SD	W08	XX60	DOL 94%, QTZ 6%	−1.04	0.02	−8.43	0.04	Sampled from blocky to saddle cloudy dolomite replacive cement in bioclastic rudstone
RTR	BD	W08	XX60	DOL 98%, QTZ 2%	0.95	0.05	−0.72	0.04	Sampled from hyaline vug-filling dolomite
RTR	BC	W10	XX11	CAL 88%, QTZ 12%	0.76	0.02	−0.74	0.02	Sampled blocky calcite replacive cement in bioclastic rudstone
RTR	BD	W13	XX16	DOL 75%, QTZ 17%, CAL 8%	0.23	0.02	−1.36	0.02	Sampled from dolostone (microcrystalline blocky dolomite)
RTR	BD	W13	XX68.1	DOL 78%, QTZ 20%	1.00	0.02	−1.18	0.04	Sampled from dolostone (microcrystalline blocky dolomite)
SRIII	BC	W14	XX75	QTZ 56%, CAL 44%	1.02	0.05	−0.75	0.03	Bulk sampling from quartz rich (detrital) and replacive blocky calcite cement
RTR	BC	W16	XX28.5	CAL 80%, QTZ 20%	−3.21	0.03	−1.54	0.03	Bulk sampling from recrystallized hybrid arenite
RTR	BC	W18	XX42.2	QTZ 61%, CAL 35%, DOL 3%	1.36	0.07	−7.01	0.16	Sampled from intraclast macrocrystalline calcite cement in chert-rich breccia
RTR	BD	W18	XX43.6	DOL 63%, QTZ 37%	1.07	0.04	−2.38	0.04	Sampled from dolostone matrix
RTR	BCv	W18	XX43.6	CAL 99%, QTZ 1%	1.02	0.02	−8.79	0.03	Manual picking of vein-filling macrocrystalline calcite
RTR	BC	W18	XX48.5	CAL 96%, QTZ 4%	0.61	0.02	−3.57	0.04	Sampled from replacive calcite cement in bioclastic rudstone
RTR	BC	W21	XX37	CAL 59%, QTZ 41%	1.37	0.04	−5.64	0.04	Sampled from calcite nodule in Mg-clay rich siltstone
RTR	BD	W21	XX44	CAL 74%, DOL 17%, QTZ 9%	−0.62	0.04	−2.68	0.03	Bulk sampling from dolostone intensively recrystallized by replacive calcite
SRI	BD	W25	XX75	ORT 78%, ANK 12%, QTZ 10%	−0.47	0.09	−4.02	0.17	Bulk sampling from arkose cemented by Fe-dolomite
RTR	BC	W33	XX08	CAL 100%	1.66	0.03	−1.76	0.03	Bulk sampling from bioclastic rudstone with replacive blocky calcite cement

BC: blocky calcite; BD, block dolomite; RTR, rift transition; s.d., standard deviation; SD, saddle dolomite; SRI and SRIII, syn-rift phases I and III, respectively; TSS, tectonic-stratigraphic stage; XRD, X-ray diffraction. XRD mineralogy: ANK, ankerite; CAL, calcite; DOL, dolomite; ORT, orthoclase; QTZ, quartz; BCv, blocky calcite in veins.

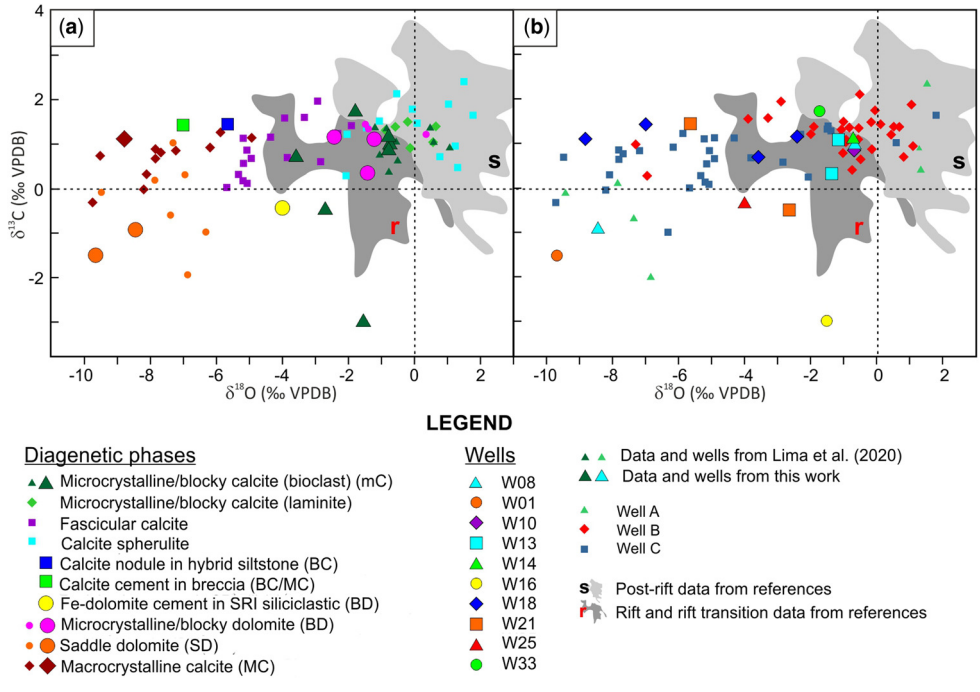

Fig. 9. O–C stable isotopes composition by (**a**) diagenetic products and (**b**) wells. In both figures, the results shown in Table 2 are represented by bigger symbols superposed onto the data compiled in Lima *et al.* (2020), represented by smaller symbols and regions that represent data from rift (r) and post-rift (s) units compiled from previous works. Notice that some diagenetic products are missing in previous publications because they were not investigated before or were not observed in this work.

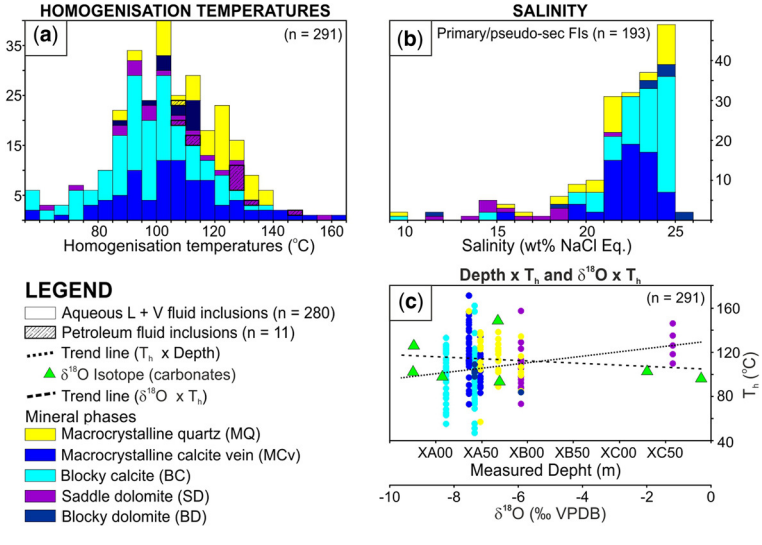

Fig. 10. (**a**) Homogenization temperature (T_h; in °C) histograms of aqueous and petroleum primary and pseudosecondary fluid inclusions (FIs) hosted in hydrothermal mineral phases. (**b**) Histogram of salinities estimated for aqueous FIs computed using the NaCl–H_2O system. Bars are coloured according to the host mineral. (**c**) Cross-plots of depth × T_h, and $\delta^{18}O$ × T_h with respective trend lines. Points representing T_h are coloured according to mineral phases. Depth increases to the right.

Table 3. Statistical summary of the results obtained in aqueous and petroleum inclusions

Well	Depth (m)	Min phase	Strat. unit (TSS)	Lithofacies	Type	UV colour (HC-bearing only)	Fill	T_{fm}	T_{hyd}	T_{ice} (°C) range	T_h (°C) range	T_h (°C) avg. (n)	Salinity (wt% NaCl eq.)	Salinity (wt% NaCl + $CaCl_2$ eq.)	Notes
W02	XX93	MQ (inner)	Bas.	Basement	AQ	–	L + V			−19.5	111	111 (1)	22		
W02	XX93	MQ (outer)	Bas.	Basement	AQ		L + V			−21.5–22.6	95–134	108 (6)	23.5–24.2		
W02	XX93	MQ	Bas.	Basement	AQ		L + V			−3.5	99–105	102 (2)	5.7		Metastable Tice
W02	XX93	MQ (inner)	Bas.	Basement	AQ		L + V			−6.5–23	111–123	116.5 (4)	9.9–24.5		
W02	XX93	MQ (inner)	Bas.	Basement	AQ		L + V				85	85 (1)			
W02	XX93	MQ (inner)	Bas.	Basement	AQ		L + V			−18.5	107	107 (1)	21.2		
W10	XX36	MQ	RTR	Bioclastic packstone (silicified)	AQ		L + V			−18.6	157	157 (1)	21.3		
W13	XX68	MQ	RTR	Chert	AQ		L + V			−11.3–22.8	112–132	124.5 (6)	15.2–24.4		
W13	XX68	MQ	RTR	Chert	AQ		L + V				104–123	116 (5)			
W13	XX68	MQ	RTR	Chert	HC	Orange	L1 + L2 + V				89–102	94 (3)			
W13	XX68	MQ	RTR	Chert	AQ		L + V			−20.1–22.4	118	118 (1)	22.4–24.1		
W13	XX68	MQ	RTR	Chert	AQ		L + V			−19.5–22.6	122	122 (2)	22.0–24.2		
W13	XX68	MQ	RTR	Chert	AQ		L + V			−22.8	121–138	129.5 (2)	24.4		
W18	XX48.3	MQ	RTR	Bioclastic rudstone	HC	Green-white	L + V				57–111	84 (2)			
W18	XX48.3	MQ	RTR	Bioclastic rudstone	AQ		L + V			−14.7	132	132 (1)	18.2		
W18	XX48.3	MQ	RTR	Bioclastic rudstone	AQ		L + V			−16.0	122	122 (1)	19.3		
W18	XX48.3	MQ	RTR	Bioclastic rudstone	AQ		L + V			−15.3–16.6	104–129	109.6 (5)	18.7–19.7		
W18	XX48.3	MQ	RTR	Bioclastic rudstone	AQ		L + V				122–136	129 (2)			
W18	XX48.3	MQ	RTR	Bioclastic rudstone	AQ		L + V			−18.2–19.2	124–131	127.6 (7)	21–21.7		
W10	XX36	MCv	RTR	Bioclastic packstone (silicified)	AQ		L + V			−19	73–90	81.8 (4)	21.6		
W10	XX36	MCv	RTR	Bioclastic packstone (silicified)	AQ		L + V			−19–20.3	85–132	113.4 (11)	21.6–22.6		
W10	XX36	MCv	RTR	Bioclastic packstone (silicified)	AQ		L + V	−52	−22.5–22.7	−18.1–20.2	114–153	132.7 (11)	20.7–22.5	17.5–18.2	
W10	XX36	MCv	RTR	Bioclastic packstone (silicified)	AQ		L + V	−52	22.5	−19.1	139–156	147.5 (2)	21.7	18	
W10	XX36	MCv	RTR	Bioclastic packstone (silicified)	AQ		L + V	−52	−21.5	−19.3	113	113 (1)	21.8	20.9	Metastable Tice
W10	XX36	MCv	RTR	Bioclastic packstone (silicified)	AQ		L + V				113	113 (1)			
W10	XX36	MCv	RTR	Bioclastic packstone (silicified)	AQ		L + V	−52	−23.8	−22.9	107–118	112.5 (2)	24.5	16.8	
W10	XX36	MCv	RTR	Bioclastic packstone (silicified)	AQ		L + V	−52	22.9–23.1	−20.2–22.8	111–147	122.8 (7)	22.5–24.4	17.7–19.5	
W10	XX36	MCv	RTR	Bioclastic packstone (silicified)	AQ		L + V	−52	−22.5	−18.5–21.5	116–145	124.5 (6)	21.2–23.5	19.5	
W10	XX36	MCv	RTR	Bioclastic packstone (silicified)	AQ		L + V			−19.7	110	110 (1)	22.1		Metastable Tice
W10	XX36	MCv	RTR	Bioclastic packstone (silicified)	AQ		L + V	−52		−19.5–22.4	109–121	112.6 (5)	22.2–24.1		
W18	XX48.3	MCv	RTR	Bioclastic rudstone	AQ		L + V			−11.3	83–106	94.3 (3)	15.2		
W18	XX48.3	MCv	RTR	Bioclastic rudstone	AQ		L + V	−52	−22.3–22.5	−20.3–21.3	96–109	104.8 (6)	22.6–23.3	18.8–19.9	
W18	XX48.3	MCv	RTR	Bioclastic rudstone	AQ		L + V			−20.8	93	93 (1)	22.9		
W18	XX48.3	MCv	RTR	Bioclastic rudstone	AQ		L + V	−52		−13.8	93–120	105.3 (3)	22.9–24.9		

W18	XX48.3	MCv	RTR	Bioclastic rudstone	AQ		L + V	−40–52.5		−21.4–22.2	89–134	107.2 (11)	23.4–23.9		
W18	XX48.3	MCv	RTR	Bioclastic rudstone	AQ		L + V	−50–52		−16.5–21.7	83–98	90.9 (14)	19.7–24.2		Some metastable FIs
W10	XX11	BC	RTR	Bioclastic rudstone	AQ		L + V	−45–52	−13.5–22.7	−16.5–22.7	65–126	95.9 (32)	19.5–24.4	19.4–21.2	
W10	XX11	BC	RTR	Bioclastic rudstone	AQ		L + V			−10.8–19.8	103–122	110 (9)	14.7–22.2		
W10	XX11	BC	RTR	Bioclastic rudstone	AQ		L + V			−5.0–10.7	93	93 (1)	7.9–14.6		
W10	XX11	BC	RTR	Bioclastic rudstone	AQ		L + V			−20.5–22.6	82–103	95.4 (5)	22.7–23.5		
W10	XX11	BC	RTR	Bioclastic rudstone	AQ		L + V			−21.8	63	63 (1)	23.7		
W18	XX42.2	BC	RTR	Bioclastic rudstone	AQ		L + V	−35–52.0	−10.0–12.0	−19.5–22.8	78–107	95.2 (17)	22.0–24.4	20.6–24.8	
W18	XX42.2	BC	RTR	Bioclastic rudstone	AQ		L + V	−40.0	−15.0	−19.8–22.1	55–106	87.3 (9)	22.2–23.9		
W18	XX42.2	BC	RTR	Bioclastic rudstone	AQ		L + V	−35		−22.1–22.5	99–103	101 (2)	23.9–24.2		
W18	XX42.2	BC	RTR	Breccia	AQ		L + V		−9.0	−19.2–22.8	75–123	99.5 (4)	21.8–24.4	21.1	
W18	XX42.2	BC	RTR	Breccia	AQ		L + V	−40	−0.5	−21.8	113	113 (1)	23.7	24.2	
W18	XX42.2	BC	RTR	Breccia	AQ		L + V	−52	−9.0–16	−22.0–22.9	157	157 (1)	23.8–24.5	20.4–21.7	
W18	XX42.2	BC	RTR	Breccia	AQ		L + V		−9.0	−18.5–23.5	73–121	92.7 (14)	21.2–24.9	21.1	
W18	XX42.2	BC	RTR	Breccia	AQ		L + V		−15.0–17.0	−22.5	87–137	107.6 (8)	24.2	20.5–20.8	
W18	XX42.2	BC	RTR	Breccia	AQ		L + V	−46.0	−13.0–15.0	−22.3–22.6	88–121	99.5 (10)	24.0–24.2	20.9–21.2	
W01	XX58.5	SD	Bas.	Basement	HC	Blueish	L + V				110–146	126.6 (9)			
W02	XX93	SD	Bas.	Basement	AQ		L + V			−10.2–13.8	73–113	95.6 (4)	14.5–17.4		Dolom. 2
W02	XX93	SD	Bas.	Basement	AQ		L + V			−10.2	88–111	98.4 (5)	14.1		Dolom. 2
W02	XX93	SD	Bas.	Basement	AQ		L + V			−8.0–18.5	87–157	121 (5)	11.7–21.2		Dolom. 2
W02	XX93	SD	Bas.	Basement	AQ		L + V			−15.0	95–113	101 (3)	18.5		Dolom. 2
W02	XX93	BD	Bas.	Basement	AQ		L + V			−22.5	111–112	111.5 (2)	24.2		Dolom. 1
W02	XX93	BD	Bas.	Basement	AQ		L + V			−16.5–23.8	97–116	109.3 (7)	23.5–25.1	12.4	Dolom. 1
W02	XX93	BD	Bas.	Basement	AQ		L + V			−22.0	84–102	96 (3)	18.6–23.8		Dolom. 1
W02	XX93	BD	Bas.	Basement	AQ		L + V	−52	−24.6	−23.9	111	111 (1)	25.2	15.3	Dolom. 1
W18	XX42.2	BD	RTR	Breccia	AQ		L + V			−16.5–22.5	97–109	104.5 (4)	23.5–24.2		

Fluid inclusions (FIs) are hosted in hydrothermal macrocrystalline quartz (MQ), replacive calcite (MC) and vein-filling macrocrystalline calcite (MCv), blocky dolomites (BD) and saddle dolomites (SD) in basement rocks (Bas.), and also in bioclastic rudstones and silicified bioclastic packstone of the rift transition sequence (RTR). For the fill, L + V means liquid + vapour and L1 + L2 + V is liquid 1 + liquid 2 + vapour. T_{fm} is the temperature of the first melting; T_{hyd} is the temperature of the hydrate melting; T_{ice} is the temperature of final ice melting; T_h is the temperature of homogenization, of which the range and average (avg.) of values are presented. Salinity (wt% NaCl eq. and wt% NaCl + $CaCl_2$ eq.) are equivalent salinities estimated using the equilibrium conditions predicted experimentally for the NaCl–H_2O and NaCl–H_2O–$CaCl_2$ systems, respectively. AQ, Aqueous; HC, HC-bearing. Dolom.1 and Dolom. 2 are based on relative timing as suggested by petrography.

The observation of very low temperatures of first melting (T_{fm}) is indicative of the presence of $CaCl_2$ in the aqueous system. Where it was possible to collect paired T_{ice} and T_{hyd} data ($n = 35$), salinities were modelled in the system NaCl–$CaCl_2$ (Naden 1996). Salinities modelled in this way tend to be similar to those calculated in the NaCl–H_2O system for 21 FIs (21–26 wt% NaCl + $CaCl_2$ eq.). However, blocky calcite has values above and macrocrystalline calcite below 20 wt% NaCl–$CaCl_2$ eq. Calculated NaCl/$CaCl_2$ ratios indicate that Na^+ is the dominant cation and NaCl/NaCl–$CaCl_2$ is typically between 0.8 and 0.9 [by weight].

T_h were compared with stable isotope data when $\delta^{18}O$ and T_h data are available for the same sample or the same mineral phase in the same well. The average T_h value for the most abundant carbonate phase was considered. Despite significant dispersion, there is a positive correlation between T_h and depletion in $\delta^{18}O$ (Fig. 10c).

U–Pb geochronology and the timing of diagenesis

Twenty Tera-Wasserburg concordia plots were obtained from selected cements in nine samples from six wellbores. They sampled crack-filled veins, vug-filling, replacive, and cements of dolomites and calcite in the crystalline basement, from SRI arkoses, RTR breccias and bioclastic rudstones. Each plot represents one analysis consisting of pooled $^{238}U/^{206}Pb$ v. $^{207}Pb/^{206}Pb$ data from a single mineral phase identified by CL imagery. Six examples of concordia plots are shown in Figure 11a–f and are focused on results obtained within the same well. To investigate potential age variations within minerals presumably from the same diagenetic phase, whenever possible analyses were conducted on various cements of the same sample (Fig. 11g–j). Besides showing clear differences within the dolomite phases (Fig. 7e–g), petrography and CL imagery were not able to distinguish calcites formed at different ages. Three of the plots were considered unsuccessful because of: (1) high common lead content; or (2) samples with analytical uncertainties that preclude regression.

Figure 12 shows a detailed compilation of the samples with geochronologic, C–O stable isotopes and FI data. They are presented from a geologic perspective, with their position reflecting the stratigraphic unit and wellbore location. Figure 13 provides a summary of measured ages, T_h from the FI study and the subsidence curve with predicted temperatures at burial conditions. The chosen T_h values occurred in the same mineral phases as those whose absolute ages were identified by U–Pb geochronology. These data are correlated to tectonic and magmatic events, and with the lithostratigraphic column of the Campos Basin (Winter *et al.* 2007; Fetter 2009). For example, blocky and macrocrystalline calcite are not grouped by age in Figure 13 because their petrographic similarity suggests they might have developed over several diagenetic stages (see Fig. 11h).

The absolute ages are clearly clustered into three intervals that coincide with the post-rift (PR) inversion (Strugale and Cartwright 2022) and with tectonic events described in the post-salt layers of the Campos Basin (Fetter 2009). These periods are interpreted as episodes of diagenetic mineral formation and recrystallization. Due to their contemporaneity with tectonic events, they are interpreted as tectono-diagenetic events, named the Barremian–Aptian (BADE; 125–117 Ma), the Albo–Cenomanian (ACDE; 103–98 Ma) and the Campanian–Maastrichtian (CMDE; 83–70 Ma). A Hauterivian age was obtained for a saddle ankerite vein in the basement, but it has over 20 Ma of uncertainty and therefore could be part of the first cluster of ages (Fig. 11j). The ages that determined the first cluster were obtained in dolomites, while the ages for the second and third cluster of ages came predominantly from calcites.

BADE ages were obtained in carbonate veins in the basement and in saddle dolomite crystals from a brecciated chert of the RTR sequence (Fig. 11a–c). The ages of 124.6 ± 1.75 Ma and 117.62 ± 4.99 Ma were collected from the blocky dolomite and saddle Fe-dolomite phases shown in Figure 11j; unfortunately, no reliable age was obtained in the ankerite gap deposit or in the breccia-fill saddle ankerite of Figure 3a. Finally, ages of 123.72 ± 2.17 Ma and 120.56 ± 2.88 Ma were measured in saddle dolomites and dolomite overgrowths in the matrix of the sample in Figure 4a (chert).

The clustered ages of BADE and the Fe-rich character of mineral phases suggest that the same fluid is likely to have percolated across the basement and RTR units under similar burial conditions. Petroleum FI data in saddle dolmites provide a T_h range of 110–146°C. These temperatures are significantly higher than the estimated values based on the subsidence curve (*c.* 70°C, Fig. 13), attesting to the imposition of a hydrothermal qualifier on BADE at shallow burial conditions (cf. Machel and Lonnee 2002).

It seems likely that the Campos Basin was under a high geothermal gradient inherited from volcanism associated with the SRI sequence, even though there does not appear to be any Barremian–Aptian age magmatism in the near vicinity. The ages of BADE are in part older than the depositional age of the hosting RTR (Coqueiros Formation) based on the traditional stratigraphic

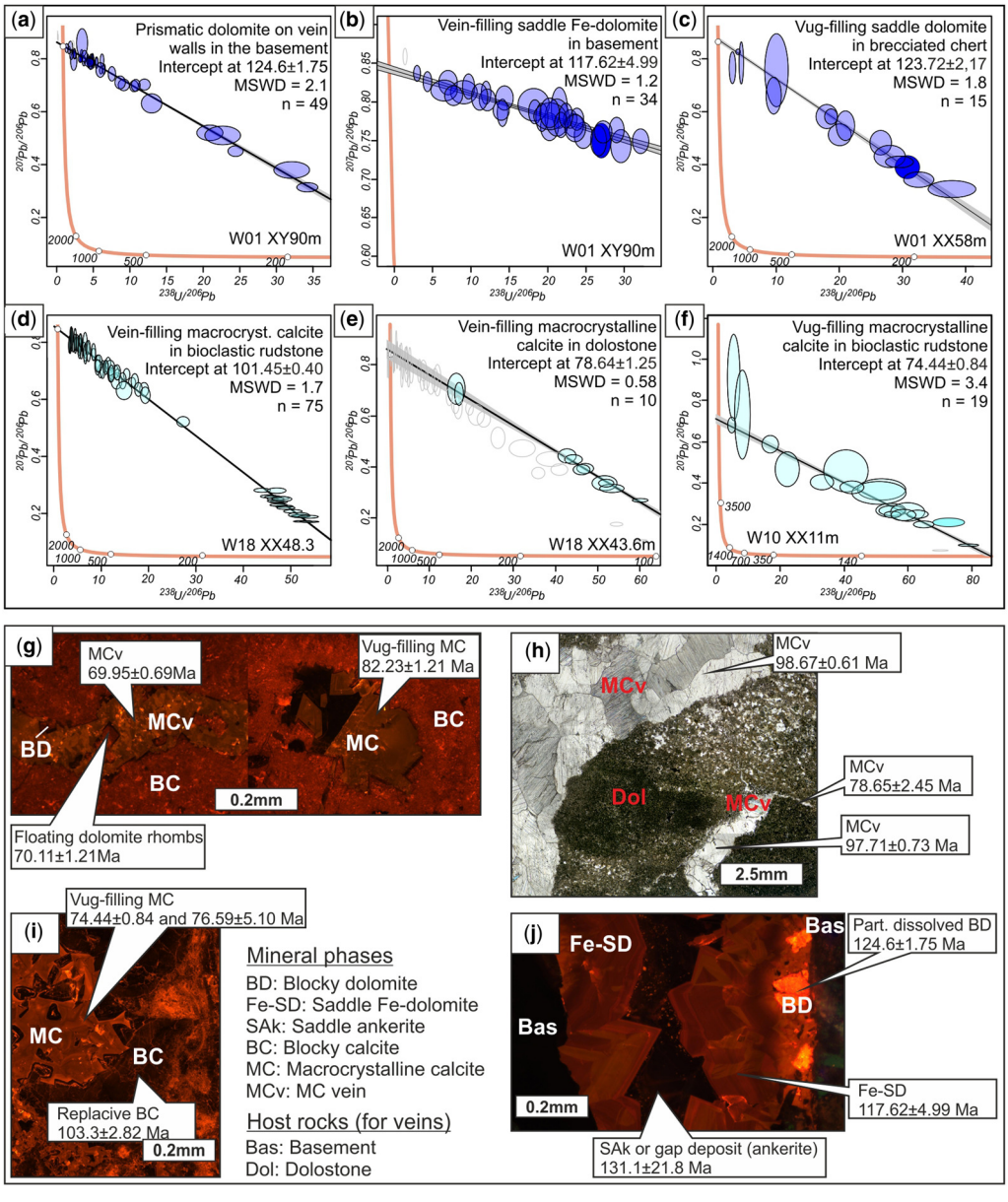

Fig. 11. (**a–f**) Tera-Wasserburg concordia plots showing pooled $^{238}U/^{206}Pb$ v. $^{207}Pb/^{206}Pb$ data for carbonate phases from samples collected in the lower section of the pre-salt interval and cements in basement rocks. Quoted age uncertainty includes propagated systematic uncertainties. Data point error ellipses are 2σ. (**g–j**) Examples of different mineral phases dated in same sample through U–Pb geochronology. (**g**) Bioclastic rudstone with vein- and vug-filling calcite (cathodoluminescence (CL) imagery). (**h**) Dolostone with two generation of MCv veins resolved by geochronology (PPL mosaic). (**i**) Bioclastic rudstone showing contrasting ages for matrix and vug-filling calcites. (**j**) Dolomite to ankerite vein filling in fractured basement. See the supplementary material for the complete explanation of the methodology and untreated results. MSWD, mean square of weighted deviates.

chart of the Campos Basin (Winter *et al.* 2007), suggesting that this unit could be older than previous interpretations.

Another characteristic of BADE is that minerals reflect a fluid enriched in Fe, which is exemplified in Figure 11j. This suggests that the fracture-fill

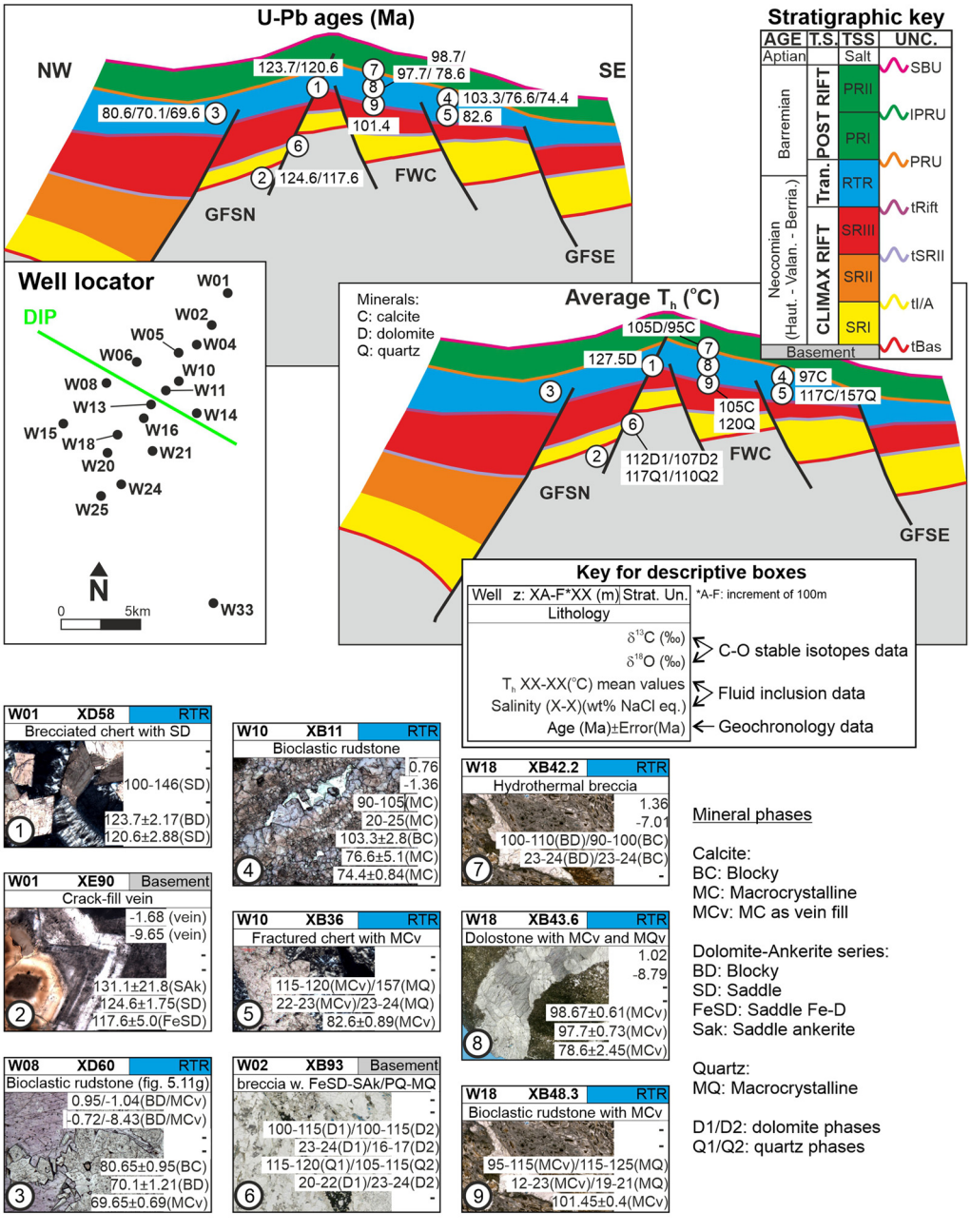

Fig. 12. At the top, a pair of summarized geological cross-sections show simplified U–Pb ages and mean homogenization temperature (T_h) for different diagenetic mineral phases from samples 1 to 9. Detailed datasets are present in the descriptive boxes at the bottom with the numbers respective to the cross-sections. Selected samples are those with geochronologic data, except for sample 7. It is shown due to its proximity to samples 8 and 9. A crop of Figure 2a is shown to contextualize the well location with the approximate position of the cross-section.

pyrite found in some samples of basement and RTR (Figs 3a & 4e) may have originated at this time rather than during the most recent diagenetic phase (Lima *et al.* 2020). Fe-rich carbonate cements are commonly formed from fluids that percolated basement, basalts and arkoses prior to reaching

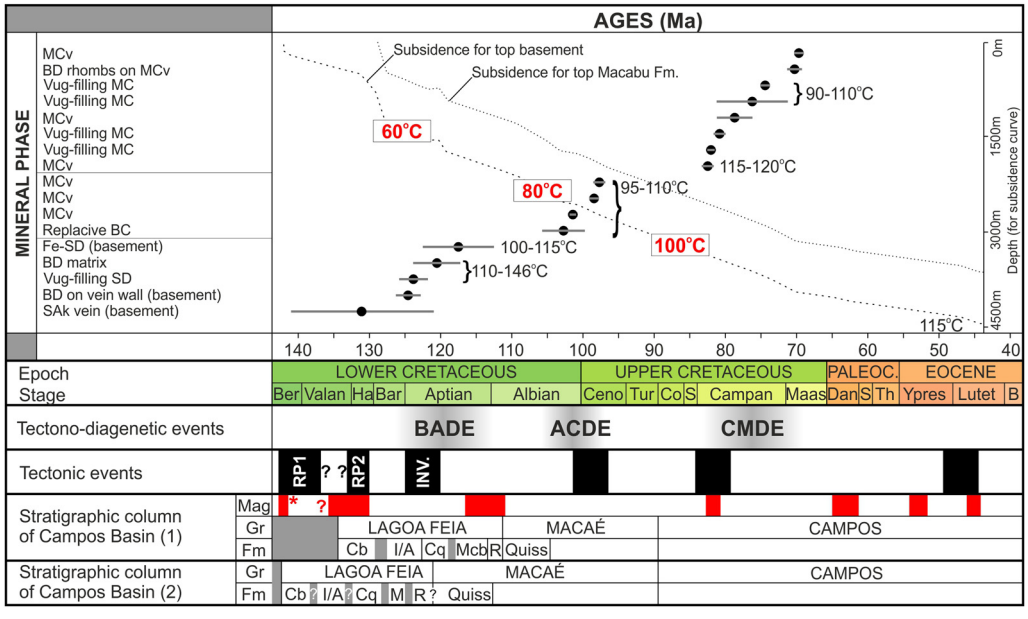

Fig. 13. Ages obtained for mineral phases identified. Temperatures in black are the homogenization temperature (T_h) intervals obtained from fluid inclusions. Ages are superimposed to subsidence curves (stippled and dotted lines) and predicted temperatures (in red) (Lima *et al.* 2020). Tectonic events rift phase (RP1) and rift phase 2 (RP2), and inversion (INV.) are according to Strugale and Cartwright (2022), while the three that follow are according to Fetter (2009). (1) Stratigraphic charts according to Winter *et al.* (2007), including the magmatic events (Mag), where * is the age of onshore tholeiitic dykes (Santiago *et al.* 2020). (2) Stratigraphic charts according to Figure 1. Cb, Cabiúnas; Cq, Coqueiros; Fm, Formations; Gr, Group; I/A, Itabapoana and Atafona; M, Macabu; Quiss, Quissamã; R, Retiro (evaporites).

sites of mineral precipitation (Everett *et al.* 1999; Dewit *et al.* 2014).

The ages that defined the ACDE were obtained from two wells where the oldest value (103.3 ± 2.82 Ma) was measured in matrix-replacing blocky calcite. Interestingly, in the same sample, vug-filling macrocrystalline calcites resulted in a younger age of 74.44 ± 0.84 Ma (Fig. 11f, i), which corresponds to the subsequent CMDE event. Three values within a system of MCv veins of 101.45 ± 0.4 Ma (Fig. 11d), 98.67 ± 0.61 Ma and 97.71 ± 0.73 Ma (Fig. 11h) were obtained from different regions. It is pertinent to emphasize that neither conventional petrography, QEMSCAN mapping nor CL imagery were able to distinguish these different generations. Individual crystals might have developed asynchronously or over a long period of time, as was the case with the quartz-filled fractures described by Lander and Laubach (2015) for quartz-filled fractures.

T_h data shows entrapment temperatures higher than those predicted by a subsidence curve of *c.* 85°C, but not as high as during BADE (Fig. 13). Nevertheless, T_h values are still at least 5°C hotter than the host rock and the diagenetic environment is thus considered hydrothermal (cf. White 1957), but at deeper burial conditions than BADE (Fig. 13). There was no magmatism recorded in the Campos Basin during the Albo–Cenomanian (Winter *et al.* 2007). Fetter (2009) observed a peak of deformation at this age in restored sections of the post-salt of the Campos Basin.

The youngest cluster of U–Pb ages spans the Campanian and most of the Maastrichtian (83–70 Ma; Fig. 13). CMDE ages came from eight pooled datasets obtained from the same samples where the ACDE was measured. With one exception (dolomite in Fig. 11g), all the data came from vein- and vug-filling calcites (Fig. 11g–i).

The petrographic descriptions show no clear paragenetic relationship between calcite formation and matrix replacement or vein filling. The latest matrix-replacing cements were identified on CL imagery as marginal, but contrasting ages on the MCv calcites were only possible from the geochronology (Figs 11e & 11f). Ages from both cements (replacive and vug-fill) and fracture-fill (macrocrystalline calcite) are indistinguishable, including a sample that contains veins related to both the ACDE and the CMDE (Fig. 11h), although the youngest ages were obtained in veins.

The time relation between U–Pb clustered ages and tectonic events suggests recurring events of matrix replacement and vug filling which could be attributed to hydrothermal diagenesis in association with brittle deformation related to structural diagenesis. Structural diagenesis is the study of the relationships between deformation or deformational structures and chemical changes to sediments (cf. Laubach *et al.* 2010). The diagenetic setting used to define each tectono-diagenetic event is a function of the local (host) temperature as suggested from the burial depth obtained from the subsidence curve, as well as the fluid temperatures obtained from FI analysis, following the classification of Machel and Lonnee (2002). Accordingly, the diagenetic settings of the BADE, ACDE and CMDE are shallow, intermediate deep and deep burial, respectively, and the hydrothermal qualifier decreases with time, reaching equilibrium during the end of the Cretaceous (Fig. 13). In brief, the differences between ambient (host rock) temperature and fluid temperature decreases throughout from the Barremian, thus the similarity in the temperatures suggested that there is no hydrothermal signature after Maastrichtian times.

Discussion

Diagenetic environments

Numerous and diverse studies are required in order to establish the definition and boundary conditions needed for diagenesis (Choquette and James 1987; Machel 1999; Morad *et al.* 2000; Klimchouk 2012). The deep burial realm (cf. Machel 1999) is perhaps the most prolonged, complex and arguably the least well understood of all diagenetic realms. A recently published review paper compares terminologies relating to diagenetic environments for marine carbonates (Immenhauser 2022). In addition, there are classifications based on temperature contrasts between the fluid responsible for mineral formation and ambient or host-rock temperature (Machel and Lonnee 2002). The terms hydrothermal and geothermal were proposed by these authors, based on the assumption that a fluid classified as hydrothermal should be at least 5–10°C hotter than the host rock (White 1957).

Most classification schemes are based on burial depth, in which a steady increase in temperature is expected as burial depth increases (e.g. Machel 1999). The diagenetic history of the Pre-Salt reservoirs of the Northern Campos Basin was described using this model (Lima and De Ros 2019; Lima *et al.* 2020). The gradual increase in burial conditions and, as a result, of temperature during thermal subsidence, has been used to explain the diagenetic evolution of the Campos Basin (Fig. 13). From the Paleocene, magmatic events in the basin increased the heat flow in the basement, triggering a fault-linked flux of hot brines that modified the rocks through extensive hydrothermal diagenesis.

The data collected during this research provided absolute ages and temperatures of crystallization of different mineral phases, from which three tectono-diagenetic events are evident, namely BADE, ACDE and CMDE (Fig. 13). Additionally, the fluid temperatures at the time of mineral formation are provided by T_h measurements taken from dated minerals, which are compared to model temperatures based on the subsidence curve. Hence, a novel setting for diagenetic environments and their geologic evolution for the pre-salt of the Northern Campos Basin during the Cretaceous is proposed (Fig. 14).

The classification of diagenetic environments (or realms) based on burial depth (Machel 1999) and the temperature contrast between mineral formation temperature (and the related fluid) and the host rock (Machel and Lonnee 2002) are the basis for the proposed diagenetic evolution shown in Figure 14. In general, the diagenetic evolution of the pre-salt sequence is characterized by a marked temperature contrast during BADE events that progressively decreases as sediments are buried, and then reaches equilibrium during the Campanian. The origin of the heat source and the fluids remain problematic and is likely to be the combination of several sources, including magmatism and the hydrodynamics of deep-seated fluids. Potential sources and their implications are discussed in Lima *et al.* (2020). In addition, when compared with the magmatic events in the Campos Basin our results suggest that these might not have been present during the events of hydrothermal diagenesis, though recurring tectonic activity almost certainly was (Figs 13 & 14).

Paragenetic sequence

The previously published paragenetic sequences assumed that subsidence leads to progressive burial or mesodiagenesis (Herlinger *et al.* 2017; Lima and De Ros 2019; Lima *et al.* 2020). The same principle was applied to the SRI sequence in the Central Campos Basin (Carvalho and De Ros 2015). Better diagenetic environment definitions were made possible with the availability of geochronologic data, and it is apparent that paragenetic evolution is not linear but rather punctuated by episodes of fracturing and fluid flow that leads to mineral dissolution and precipitation (Figs 13 & 14). Hence, a new age-constrained paragenetic evolution for the basement and SRI sediments is proposed, as well as for the SRIII + RTR sequences (Fig. 15). This paragenetic relationship could be useful to reinterpret the mineral paragenesis using the geochronologic framework here interpreted for the PR Macabu Formation by

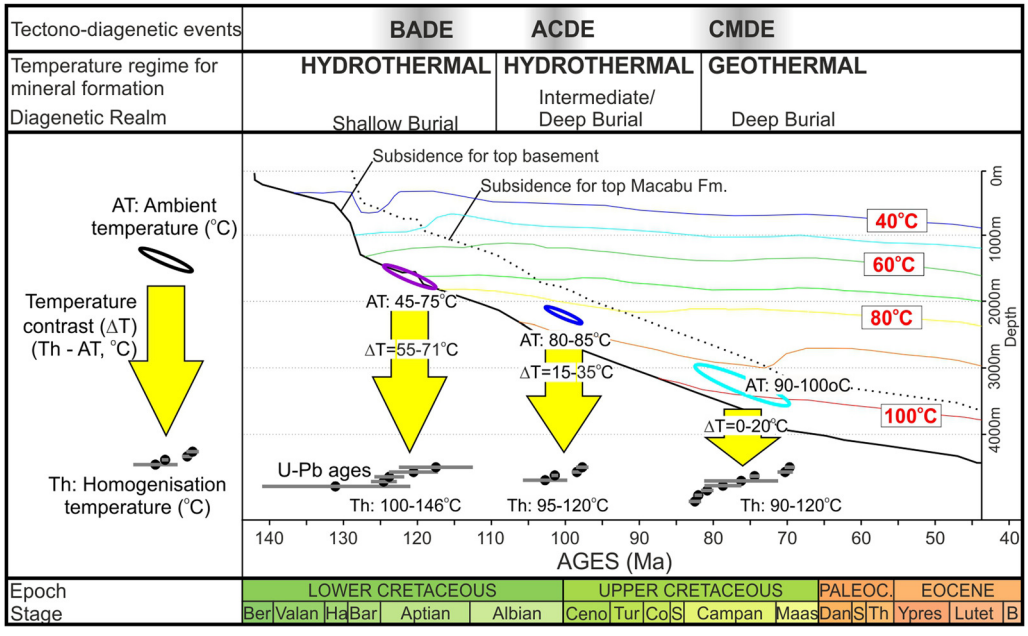

Fig. 14. Interpretation of the tectono-diagenetic events with respect to diagenetic realms (cf. Machel 1999) and the temperature regime for mineral formation or hydrothermal qualifier (cf. Machel and Lonnee 2002). The diagenetic realms are based only on the burial depth at the time of diagenesis. Ambient temperatures (AT) were taken from subsidence and temperature curves with respect to depth (adapted from Lima *et al.* 2020). Temperature contrast (Th–AT) indicates the intensity of the hydrothermal qualifier.

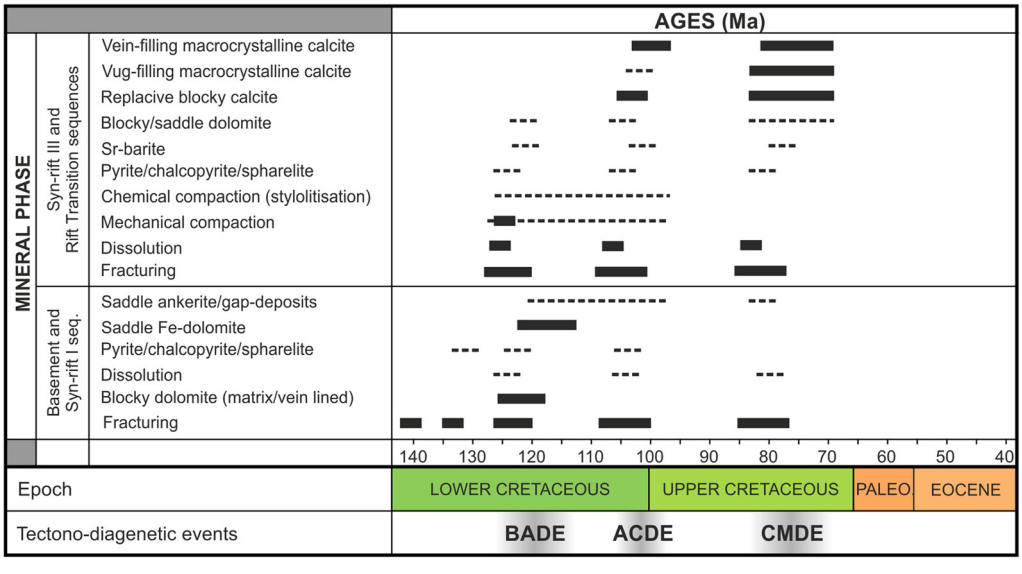

Fig. 15. Interpretation of the paragenetic evolution of the main mineral phases and processes investigated in this study compared with the tectono-diagenetic events. Mineral phases are subdivided accordingly to the geological unit. Thick bars for carbonate minerals and tectonic deformation reflect the geochronological constraints of Figure 13. ACDE, Albo–Cenomanian diagenetic event; BADE, Barremian–Aptian diagenetic event; CMDE, Campanian–Maastrichtian diagenetic event.

conventional petrography in previous publications (Herlinger *et al.* 2017; Lima and De Ros 2019; Lima *et al.* 2020).

Fracturing and dissolution probably occur contemporaneously with diagenetic phases for each event because mineral formation occurs concurrently with deformation events in the basement (Fetter 2009; Strugale *et al.* 2021). Therefore, it is assumed that the pre-salt sequence is mechanically coupled to the basement despite any strain partitioning that might be related to contrasts in mechanical proprieties (Turner and Williams 2004). Consequently, strain propagated throughout the whole section results in fault reactivation and related fracturing in the fault-related damage zones of both the basement and sedimentary section (Kelly *et al.* 1999; Walsh *et al.* 2018). In addition, mechanical coupling suggests that stress affected the whole sedimentary section, leading to widespread fracturing and subsequent mineral precipitation and recrystallization. Evidence for this is the network of calcite veins formed during two diagenetic events in the same sample (Fig. 11f).

Despite the relatively well constrained diagenetic evolution presented in Figure 15, the age of emplacement of pyrite, chalcopyrite and sphalerite remains unclear and could have happened during either BADE or ACDE events, or both. Therefore, it is recommended that pyrite nodules in clay-rich lithologies, as well as fracture/vug-filling in basement and carbonates, should be the subject of a geochronological study based on the Re–Os system (see Creaser *et al.* 2002 and Hnatyshin *et al.* 2020).

Diagenetic evolution and controls

The BADE has a hydrothermal character ($\Delta T = 55$–$70°C$) and occurred during or just after deposition of the PR sequence (Fig. 14) and has important implications for the depositional ages of the pre-salt sequence. According to Winter *et al.* (2007), the deposition of the Coqueiros Formation occurred at *c.* 122–123 Ma, which is close to ages obtained in the vug- and vein-filling dolomites of BADE (Fig. 11j). Furthermore, T_h values from petroleum FIs in these dolomites are $>110°C$ and consequently likely to be related to a hitherto unknown burial event which would also have affected the maturation of organic matter (e.g. Davies and Smith 2006). Therefore, BADE ages are interpreted to favour recent publications that consider both the Macabu and Coqueiros formations as Barremian in age (Tedeschi *et al.* 2019; Pietzsch *et al.* 2020; Strugale and Cartwright 2022) (Figs 1b & 13).

Mantle plume-induced thermal anomalism during the early break-up of the South Atlantic Ocean resulted in lithospheric thinning, rifting and an anomalous thermal gradient (Chang *et al.* 1992; Moulin *et al.* 2010). The Campos Basin was initially magma poor, but then became magma rich as oceanic crust formed in Albian times (Morgan *et al.* 2020). However, the Cabiúnas volcanics are part of the SRI sequence (Fig. 1b) and are dated at 136–130 Ma (Mizusaki *et al.* 1992). It is therefore suggested that there is no magmatic event coeval with the BADE. Magmatic events have been considered the primary heat source for diagenetic hydrothermal fluids in the Campos Basin (Herlinger *et al.* 2017; Lima and De Ros 2019), but despite the cooling that occurred at the end of the Cabiúnas volcanism, heat flow was probably still significant during the BADE. A tectonic event is still considered necessary to provide the pathways for hydrothermal fluids from a deep-seated realm to the sedimentary section. Davies and Smith (2006) noted the role of transtensional faults as ideal sub-vertical conduits for hydrothermal fluids, connecting a deep-seated setting to the shallower sections. The tectonic regime that operated during the two rift phases was transtensional, where basement structures were reactivated and could have connected deep-seated fluids to the newly deposited pre-salt sediments (Strugale *et al.* 2021; Strugale and Cartwright 2022). However, only one, highly uncertain, age related to the rift phase (131.1 $\pm$ 21 Ma) was obtained and therefore there is little evidence for syn-rifting hydrothermal diagenesis.

A common pathway for hot fluids is active faults operating through the fault-valve mechanism (cf. Sibson 1981, 1992). Strugale and Cartwright (2022) also recognized deformation related to selective reactivation of rift faults along the Guriri Fault System during the PR phase, which likely lasted until the end of the Albian. Therefore, it is suggested that the BADE could be related to PR inversion and, more importantly, that U–Pb ages represent evidence of this inversion because dated minerals were emplaced in fractures and breccias in the basement (Fig. 13). This also indicates that the basement was involved in PR deformation. In addition, it also suggests that active near-surface hydrothermal venting formed the fault-controlled mounds identified in the PRII sequence (Strugale and Cartwright 2022).

The occurrence of hydrothermal venting coeval with the deposition of the Macabu Formation is likely to have resulted in deposits related to subaerial and subaqueous hydrothermal vents despite basin-scale geochemical data not being conclusive (Pietzsch *et al.* 2018; Pietzsch *et al.* 2020). In addition, mantle-derived CO_2 is interpreted as the carbon source for hydrothermal diagenesis (Lima *et al.* 2020), and magmatic-related hydrothermal-venting complexes were identified in the shallow water domain of the Campos Basin (Alvarenga *et al.* 2016). Finally, based on the analogue of present-day lacustrine carbonates (Bischoff *et al.* 1993; Dekov *et al.* 2014), fault-related hydrothermal-venting

mounds were interpreted as being common as reservoir-scale geobodies in the Santos Basin (Barnett *et al.* 2018; Fetter *et al.* 2018).

Intensive silicification, often resulting in extensive layers spanning tens to hundreds of metres, represents the predominant hydrothermal diagenetic phenomenon observed in the Pre-Salt reservoirs of the Campos, Santos and Kwanza basins (Vieira de Luca *et al.* 2017; Tritlla *et al.* 2018; Lima and De Ros 2019; Lima *et al.* 2020). Its relative timing with respect to the carbonate phases is difficult to establish. Figure 5c, d suggest alternation of carbonate- and silica-rich fluids along time, but the relative order is unclear. Similar values of T_h and salinity from FIs also point in this direction, thus suggesting an evolution of the fluid chemistry through time.

Dolomitization, although less pronounced, consistently precedes silicification (Lima and De Ros 2019). Moreover, an examination of the spectral gamma ray logs has revealed the presence of atypical U concentration within the intensely silicified intervals. Plausibly, this U anomaly might be linked to the occurrence of APS group minerals (Sr and Al phosphates and sulfates), exemplified by svanbergite whose chemical composition allows for U diadochy (Lima *et al.* 2020). Nonetheless, it is imperative to undertake further comprehensive investigations to unequivocally establish the veracity of this option.

The minerals considered 'exotic' in the carbonate samples are described as pyrite, chalcopyrite, sphalerite, Sr-barite and svanbergite (Fig. 4c, e–f & 6b). For basement samples, the dolomite–ankerite series and pyrite-filling fractures can also be considered 'exotic' (Fig. 7e–g). This mineral suite was initially considered to be the latest diagenetic phase (Herlinger *et al.* 2017). Our interpretation is that it could be part of any of the diagenetic events (Fig. 13), but more likely related to the BADE and/or the ACDE (Fig. 15). Stable isotopes and FI studies were used to classify this phase as hydrothermal (Lima and De Ros 2019; Lima *et al.* 2020). The CMDE is mostly likely of a non-hydrothermal nature because of the lack of a temperature contrast between host rock and fluid. Nevertheless, this does not exclude it as a potential source for the hydrothermal fluids. In addition, T_h for Sr-barite ranges between 125 and 135°C (Lima *et al.* 2020), which is compatible with the T_h observed during the BADE. Pyrite is clearly earlier than Sr-barite in carbonates and it is the earliest filling stage of basement fractures (Fig. 4b). Therefore, it is suggested that the 'exotic' mineral suite is likely to be coeval with the BADE and is potentially the last mineral generating event. However, temperature and burial conditions during the ACDE and CMDE do not exclude the possibility of both sulfide and sulfate precipitation (Fig. 15).

During the ACDE, another pulse of hydrothermal diagenesis occurred, characterized by lower temperature fluids (Fig. 14). The ACDE, similar to the BADE, isn't related to magmatism but rather to a tectonic event that may be seen in the post-salt succession (Fetter 2009). As seen in the BADE, the lack of coeval volcanism suggests that deep-seated fluids of hydrothermal character could have been released during sub-seismic-scale reactivation of faults in both the basement and pre-salt section (Sibson 1981; Eichhubl and Boles 2000; Bezerra *et al.* 2021). Although episodes of intrusive and extrusive magmatism occurred during the Late Cretaceous in the Campos Basin (Thomas Filho *et al.* 2000; Matos 2021), their effect on the thermal profile of the sedimentary column was apparently limited in extent. However, due to the lack of comprehensive sampling in many parts of the Campos Basin, it is currently impossible to entirely ignore the existence of yet undiscovered magmatic events. Consequently, further in-depth studies are imperative to confirm the absence of any link between magmatic events and the origin of hydrothermal fluids.

For the CMDE, the latest diagenetic event, the volcanism interpreted as responsible for triggering hydrothermal diagenesis in the pre-salt of the Campos Basin is validated (Lima *et al.* 2020). Moreover, the CMDE is also coeval with a tectonic event described in the post-salt sequence (Fetter 2009) (Fig. 13). However, T_h values show a slight overall cooling during the Cretaceous, with fluid temperatures within the hydrothermal event observed to be consistent with the predicted burial temperature towards the end of the CMDE. Therefore, the CMDE is described as a geothermal diagenetic event taking place at 3–4 km depth (Fig. 14). This geothermal classification refers to minerals formed at similar temperatures to the host rocks (Machel and Lonnee 2002). Accordingly, the term 'geothermal' could be omitted unless special emphasis needs to be placed on the nature of the mineralization event. Therefore, for comparative purposes, the CMDE is referred to as geothermal in the present study. However, because of inherent uncertainties in temperature measurements of both FIs and predicted burial, further studies are required to conclusively rule out any potential hydrothermal origin for the CMDE. Additionally, it should be noted that T_h obtained from FIs represent only the minimum trapping temperatures. Therefore, it is likely that the paragenesis of the CMDE precipitated at temperatures higher than those measured by T_h. Finally, despite the coeval magmatism and the CMDE, it remains likely that hydrothermal or geothermal diagenetic events in the Campos Basin are dependent on tectonic and not magmatic events. The relation between magmatism and the various tectonic events is a question that remains open.

Replacive and vein-filling cements coeval with fracturing, but without a clear input of hydrothermal

fluids as suggested by the CMDE, are not evident. Compaction of pore in clastic sediment is viewed as either a mechanical or coupled mechanical–chemical, process during which mineral content and diffusion are fundamental controls on the constitution of the cements (Pingitore 1982; Bjørlykke 1999). More recently, Laubach *et al.* (2010) proposed the term 'structural diagenesis', which aims to combine deformation and chemical changes in sediments. This concept was further explored in a review paper in which fracture patterns can be interpreted as chemical transformations in a mechanical context in which fractures could remain open for over 40 Ma (Laubach *et al.* 2019). Thus, the contemporaneity of tectonic and diagenetic events, combined with extensive replacive and fracture-filling mineralization without coeval basin-scale magmatism (Figs 13–15), militate in favour of structural diagenesis for the pre-salt sequences of the Northern Campos Basin.

Structural diagenesis also involves chemical reactions that are coeval with deformation. In this study, the cements and fracture-fill that either mimic or differ from the host rock mineralogy are common in both the ACDE and CMDE. Calcite is by far the predominant cement, and there is no occurrence of this mineral phase in the sequence that predates 103 Ma (Fig. 13). On the other hand, vein- and vug-filling dolomites are the principal carbonate phases related to the BADE, with both sulfates and sulfides occurring (Fig. 15). The progressive increase in the Fe content in the dolomites of BADE (Fig. 7e–g) suggests an increasing Fe enrichment in the fluid that ultimately resulted in precipitation of pyrite, chalcopyrite and sphalerite. It was not possible to conclude if such enrichment in Fe was the effect of a more efficient hydrothermal flow bringing Fe from the basement and SRI, or whether it simply reflects the proximity of studied samples to these units. As observed in Lima *et al.* (2020), mineralogy, T_h and salinity are compatible with MVT ore deposits (Paarlberg and Evans 1977; Leach *et al.* 2005), although the close relation with normal faults makes this case more similar to the Irish subtype (Hitzman and Beaty 1996; Hitzman *et al.* 2002; Wilkinson *et al.* 2005). MVT-type deposits are notable examples of basinal fluids being circulated at basin-scale dimension.

Depositional, diagenetic and hydrothermal events along the continental margins of the South Atlantic Ocean

U–Pb geochronology has been recently used to date carbonate cements and reveal diagenetic, tectonic and magmatic events in different positions along the Atlantic Ocean (Roberts and Walker 2016; Rochelle-Bates *et al.* 2021; Ganade *et al.* 2022). Regarding the Central Segment of the South Atlantic Ocean (cf. Moulin *et al.* 2010), the U–Pb ages presented in this work are novel for the Campos Basin but have been used to study depositional and diagenetic cements in the adjacent Santos Basin (Lawson *et al.* 2022; Rochelle-Bates *et al.* 2022; Fig. 1a) and also in its African counterpart, the Namibe Basin (Rochelle-Bates *et al.* 2021). Figure 16 presents a geochronologic and geographic frameworks comparable studies and is compared with the ages and tectono-diagenetic events described in this work.

For the Santos Basin, Lawson *et al.* (2022) obtained ages of 115.83 $\pm$ 1.65 Ma (isotope dilution thermal ionization mass spectrometry (ID-TIMS) U–Pb dating), 114.46 $\pm$ 4.72 Ma and 109.73 $\pm$ 9.26 Ma (LA-ICP-MS dating) – interpreted as the depositional age of the Barra Velha Formation, the equivalent of the Macabu Formation in the Campos Basin. A similar age was obtained in carbonate shrubs and spherulites of the Barra Velha Formation, where U–Pb LA-ICP-MS dating yields a pooled age of 106.9 $\pm$ 4.3 Ma (Rochelle-Bates *et al.* 2022). However, the latter have interpreted these ages as diagenetic and not depositional. Regardless of their interpretation, these ages occur between the BADE (125–118 Ma) and the ACDE (103–98 Ma; Fig. 16). It is relevant to note that these ages were obtained in cements formed under shallow- to intermediate-burial conditions (between 1 and 2 km) and are thus clearly diagenetic (Fig. 14).

Younger hydrothermal cements were found in the pre-salt rocks of both the Santos and Namibe basins (Rochelle-Bates *et al.* 2021, 2022), where an Upper Cretaceous magmatic-related hydrothermal diagenesis, with ages of 82–74 and 90–80 Ma, respectively, have been detected. These ages are similar to our CMDE (Fig. 16). Even younger Paleocene ages were obtained in both the Santos (59.2 $\pm$ 5.3 and 58.0 $\pm$ 4.6 Ma) and Namibe (56.8 $\pm$ 4.8 Ma) basins (Rochelle-Bates *et al.* 2021, 2022). Fetter (2009) used balanced sections to describe a peak of deformation with a similar age in the post-salt of the Campos Basin (Fig. 13). The lack of Paleocene to Eocene diagenetic events in the Northern Campos Basin could be related to sampling bias, which may not have sampled the equivalent cement studied here.

These observations suggest that tectonism, magmatism and enhanced diagenesis could be controlled by regional-scale tectonics because similar diagenetic ages were observed along both margins of the Central Segment in the South Atlantic Ocean regardless of coeval magmatic events. Given the symmetry between the margins, regional tectonic events could be attributed to episodes of increasing oceanic spreading, possibly also reflecting the evolving dynamics of the Andean Orogen. Intraplate tectonics is an important mechanism for the deformation of both intracratonic and continental-margin basins of the South American continent during the

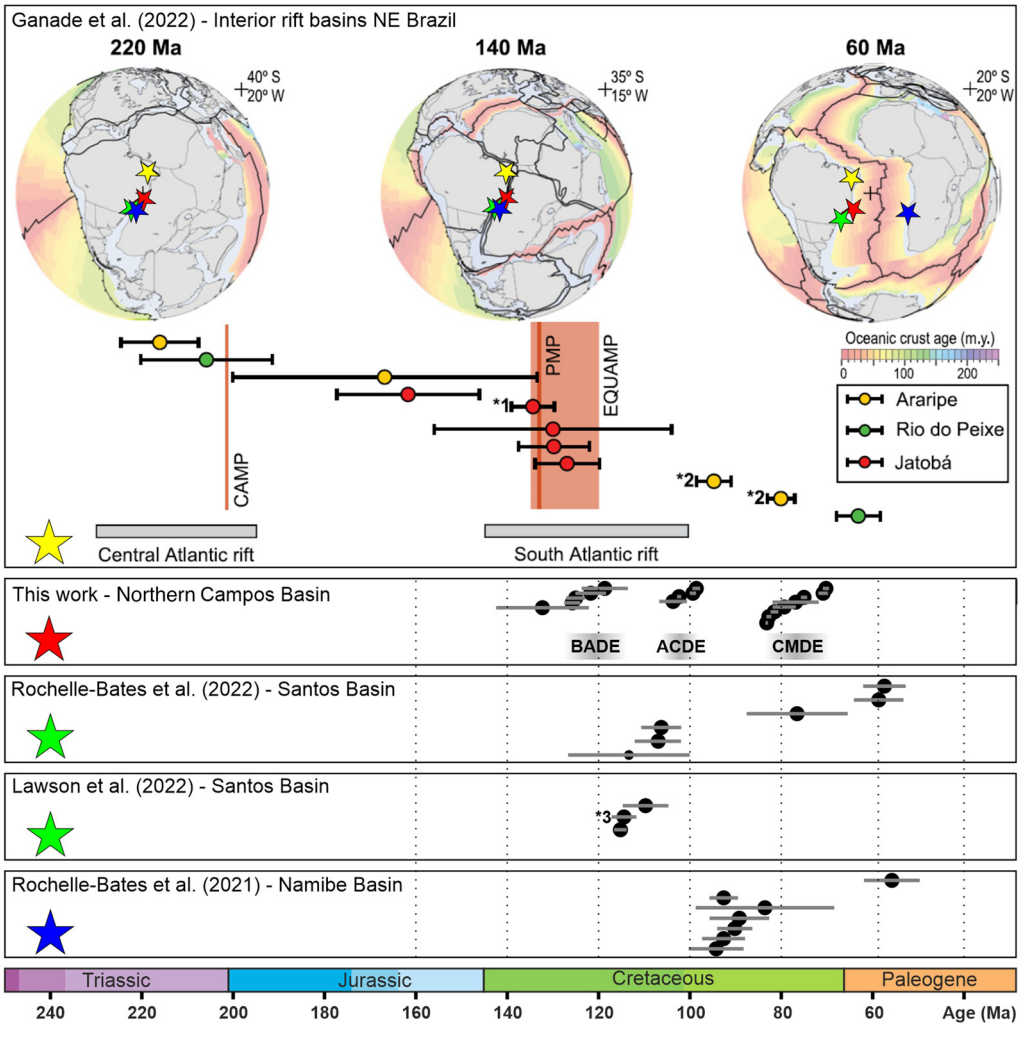

Fig. 16. Compilation of the geochronologic data from diagenetic carbonate cements available for the Brazilian Margin (Ganade *et al.* 2022; Lawson *et al.* 2022; Rochelle-Bates *et al.* 2022) and Namibe Basin (Rochelle-Bates *et al.* 2021) compared with the results of this work (Figs 12 & 13). At the top is shown the plate configuration in three key moments of the Atlantic rifting and ages obtained across the interior rift basins of NE Brazil, named Araripe, Rio do Peixe and Jatobá, by Ganade *et al.* (2022) and (Miranda *et al.* 2020; Celestino *et al.* 2021) references therein. Coloured stars are the approximate location of the studied areas during the margin evolution with respect to the South Atlantic opening. All data were obtained through laser ablation inductively coupled plasma mass spectrometry (LA-ICP-MS), except *3, which was obtained by U–Pb isotope dilution. CAMP, Central Atlantic magmatic province; EQUAMP, Equatorial Atlantic magmatic province; PMP, Paraná magmatic province.

Phanerozoic (Assumpcao 1992; Cobbold *et al.* 2007; Milani and De Wit 2008; Bezerra *et al.* 2011). Despite the good temporal correlation between orogenic pulses in the Andean Orogen with tectonic and magmatic events in the South Atlantic (Cobbold *et al.* 2007; Mohriak *et al.* 2008), other workers have justified these events based only on pulses of more rapid oceanic spreading in the Meso-Atlantic chain (Kukla *et al.* 2018). Fetter (2009) interpreted three tectonic events that affected the post-salt package in the Central Campos Basin, namely during the Albian, Campanian and Paleocene, and these can be correlated with the clustered ages and tectono-diagenetic events evident from this study (Figs 12 & 13). However, Fetter (2009) did not allude to the causative mechanism.

Regarding the clustering of ages obtained from diagenetic cements seen in Figure 16, two patterns

are observed: while Paleocene ages are well clustered around the interval of 60–50 Ma in the Santos, Namibe and Rio de Peixe basins, early and late Cretaceous ages are scattered and cannot be correlated across the ocean. Firstly, the earliest diagenetic cements dated in the Namibe Basin are at least 10 Ma younger than the ages obtained in the Santos Basin and around 30 Ma younger than the BADE, whereas Cretaceous diagenetic ages across the Santos and Campos basins are quite similar; the ACDE and CMDE are in phase with clustered ages for Santos Basin (Fig. 16). Regarding the BADE, although marginally time-related to the earliest cements of the Santos Basin, it is also correlated (though younger) to 140–125 Ma ages of diagenetic cements dated by LA-ICP-MS in NE Brazil (Ganade *et al.* 2022). The latter ages are in turn correlated with the 135–120 Ma Equatorial Atlantic Magmatic Province (EQUAMP) (Hollanda *et al.* 2019) and the 135–134 Ma Paraná-Etendeka Province (Rocha *et al.* 2020). If all the geochronologic data from diagenetic cements of the Brazilian Margin are assembled (Fig. 16), they suggest that earliest diagenetic-related cements are progressively younger southwards, and perhaps follows a continent-scale pattern of tectonic events whose loci migrated from north to south during Mesozoic times. Such a pattern does not appear to follow the magmatic events in terms of location and ages, and suggests a southward strain migration.

Conclusions

The crystalline basement, SRI volcanoclastics and arkoses, SRIII and RTR sediments are described as host rocks and diagenetic products.

Wellbore samples from the Northern Campos Basin reveal a complex paragenetic evolution. Basement and SRI show Fe-rich dolomites, pyrite and quartz as diagenetic products. SRIII and RTR have a wide predominance of quartz and calcite. Locally, chalcopyrite, pyrite, sphalerite and Sr-barite constitute a distinct phase that have similarities with Irish MVT Zn–Pb ore deposits.

FIs in quartz, calcite and dolomite cements revealed T_h in the range 90–130°C and correlate to present-day depths. Fluids are moderately to highly saline (>21 wt% NaCl eq. and >15 wt% NaCl–$CaCl_2$ eq.), and stable $\delta^{13}C$ values in carbonate cements are clustered between –1.68 and 1.66‰, while $\delta^{18}O$ exhibits a greater variation (between 0 and −10‰ VPDB (Vienna Peedee Belemnite isotope) reference). The lowest $\delta^{18}O$ in carbonates are correlated with higher T_h and latest diagenetic phases (veins and vug-fillings).

The U–Pb ages of replacive and vein-filling cements reveal three tectono-diagenetic events, namely the BADE (125–117 Ma), ACDE (103–98 Ma) and CMDE (83–70 Ma). These events were coeval with regional tectonic events related to basin inversion as results of propagation of intraplate stress that affected the crystalline basement and overlain sedimentary section. There was no apparent correlation between magmatic and diagenetic events.

Each of the tectono-diagenetic events occurred under contrasting diagenetic settings. A hydrothermal qualifier complementary to burial depth is needed to describe the temperature contrast between fluid and host rock at the time of diagenesis. Therefore: the BADE is hydrothermal, shallow burial; the ACDE is hydrothermal, intermediate to deep burial; and the CMDE is (geothermal) deep burial.

The tectonic events leading to fault reactivation and fracturing allowed hot basinal brines to move upward along faults, but also created fracture networks within the sedimentary layers that enhanced the lateral flow of these brines. Therefore, tectonism is interpreted as the trigger process for the diagenetic episodes. Contemporaneous tectonic and diagenetic events are interpreted as examples of structural diagenesis (cf. Laubach *et al.* 2010).

U–Pb geochronology has been deployed here as a fundamental tool to recognize tectonic events that affected carbonate sedimentation, extending the limited number of previous studies worldwide that have used this dating technique in this way. The observation of carbonates that are side by side, indistinct under the petrographic microscope and with same QEMSCAN signature, but showing ages 20 Ma apart, demonstrated the importance of the geochronology to refine the relative order of some of the paragenetic products.

Acknowledgements The authors acknowledge Petrobras S.A. for financial support throughout this project, and the Brazilian Agency of Petroleum, Gas and Biofuels to madk available the rock and seismic data here used. MS acknowledges the Department of Earth Sciences and Wolfson College, University of Oxford, for academic support, and several colleagues from Petrobras E&P and Petrobras Research Centre (CENPES) for the thoughtful discussions and suggestions. Finally, we acknowledge the constructive comments given by two reviewers, Ana Paula Coura and Langhorne Smith, and the volume editor Paul Wright.

Competing interests The authors declare that they have no known competing financial interests or personal relationships that could have appeared to influence the work reported in this paper.

Author contributions **MS**: conceptualization (lead), data curation (lead), investigation (lead), project administration (lead), writing – original draft (lead); **BEML**: validation (equal), visualization (equal), writing – review & editing (equal); **CD**: formal analysis (equal),

methodology (equal), validation (equal); **JO**: investigation (equal), validation (equal); **JR**: investigation (equal), validation (equal); **JPRO**: validation (equal), writing – review & editing (supporting); **JB**: investigation (equal), validation (equal); **LR**: methodology (equal), supervision (lead), validation (equal), writing – review & editing (equal); **NR**: formal analysis (equal), investigation (equal), validation (equal), writing – review & editing (supporting); **JC**: conceptualization (lead), formal analysis (equal), supervision (lead), validation (lead), writing – review & editing (equal).

Funding M Strugale thanks Petrobras for funding.

Data availability All data generated or analysed during this study are included in this published article (and, if present, its supplementary information files). The rock samples used are property of the Brazilian Agency of Oil and Gas and can be requested directly for research purposes.

References

Alvarenga, R., Iacopini, D., Kuchle, J., Scherer, C. and Goldberg, K. 2016. Seismic characteristics and distribution of hydrothermal vent complexes in the Cretaceous offshore rift section of the Campos Basin, offshore Brazil. *Marine and Petroleum Geology*, **74**, 12–25, https://doi.org/10.1016/j.marpetgeo.2016.03.030

Assumpcao, M. 1992. The regional intraplate stress field in South America. *Journal of Geophysical Research: Solid Earth*, **97**, 11 889–11 903, https://doi.org/10.1029/91JB01590

Barnett, A.J., Obermaier, M., Amthor, J., Juk, K., Camara, R., Sharafodin, M. and Bolton, M. 2018. Origin and significance of thick carbonate grainstone packages in non-marine successions: a case study from the Barra Velha Formation, Santos Basin. AAPG Search and Discovery article #11 116. Adapted from a poster presentation given at the AAPG Annual Convention and Exhibition, Salt Lake City, Utah, 20–23 May 2018.

Bezerra, F.H., do Nascimento, A.F., Ferreira, J.M., Nogueira, F.C., Fuck, R.A., Neves, B.B.B. and Sousa, M.O. 2011. Review of active faults in the Borborema Province, Intraplate South America – integration of seismological and paleoseismological data. *Tectonophysics*, **510**, 269–290, https://doi.org/10.1016/j.tecto.2011.08.005

Bezerra, F.H., Balsamo, F. *et al*. 2021. Hydrothermal silicification in the intraplate Samambaia seismogenic fault, Brazil: implications for fault loss of cohesion and healing in rifted crust. *Tectonophysics*, **815**, 229 002, https://doi.org/10.1016/j.tecto.2021.229002

Bischoff, J.L., Stine, S., Rosenbauer, R.J., Fitzpatrick, J.A. and Stafford, T.W., Jr 1993. Ikaite precipitation by mixing of shoreline springs and lake water, Mono Lake, California, USA. *Geochimica et Cosmochimica Acta*, **57**, 3855–3865, https://doi.org/10.1016/0016-7037(93)90339-X

Bjørlykke, K. 1999. An overview of factors controlling rates of compaction, fluid generation and flow in sedimentary basins. *In*: Jamtveit, B. and Meakin, P. (eds) *Growth, Dissolution and Pattern Formation in Geosystems*. Springer Dordrecht, 381–404.

Bustillo, MÁ. 2010. Silicification of continental carbonates. *Developments in Sedimentology*, **62**, 153–178, https://doi.org/10.1016/S0070-4571(09)06203-7

Carminatti, M., Wolff, B. and Gamboa, L. 2008. New Exploratory Frontiers in Brazil. Society of Petroleum Engineers 19th World Petroleum Congress, Madrid, Spain.

Carvalho, A.S.G. and De Ros, L.F. 2015. Diagenesis of Aptian sandstones and conglomerates of the Campos Basin. *Journal of Petroleum Science and Engineering*, **125**, 189–200, https://doi.org/10.1016/j.petrol.2014.11.019

Celestino, M.A.L., Miranda, T.S. *et al*. 2021. Structural control and geochronology of Cretaceous carbonate breccia pipes, Crato Formation, Araripe Basin, NE Brazil. *Marine and Petroleum Geology*, **132**, 104–116, https://doi.org/10.1016/j.marpetgeo.2021.105190

Ceraldi, T.S. and Green, D. 2017. Evolution of the South Atlantic lacustrine deposits in response to Early Cretaceous rifting, subsidence and lake hydrology. *Geological Society, London, Special Publications*, **438**, 77–98, https://doi.org/10.1144/SP438.10

Chang, H.K., Kowsmann, R.O., Figueiredo, A.M.F. and Bender, A.A. 1992. Tectonics and stratigraphy of the East Brazil Rift System: an overview. *Tectonophysics*, **213**, 97–138, https://doi.org/10.1016/0040-1951(92)90253-3

Choquette, P. and James, N. 1987. Diagenesis in limestones: the deep burial environment. *Geoscience Canada*, **14**, 3–35.

Cobbold, P.R., Rossello, E.A., Roperch, P., Arriagada, C., Gómez, L.A. and Lima, C. 2007. Distribution, timing, and causes of Andean deformation across South America. *Geological Society, London, Special Publications*, **272**, 321–343, https://doi.org/10.1144/GSL.SP.2007.272.01.17

Corbella, M., Ayora, C. and Cardellach, E. 2004. Hydrothermal mixing, carbonate dissolution and sulfide precipitation in Mississippi Valley-type deposits. *Mineralium Deposita*, **39**, 344–357, https://doi.org/10.1007/s00126-004-0412-5

Creaser, R.A., Sannigrahi, P., Chacko, T. and Selby, D. 2002. Further evaluation of the Re-Os geochronometer in organic-rich sedimentary rocks: a test of hydrocarbon maturation effects in the Exshaw Formation, Western Canada Sedimentary Basin. *Geochimica et Cosmochimica Acta*, **66**, 3441–3452, https://doi.org/10.1016/S0016-7037(02)00939-0

Davies, G.R. and Smith, L.B., Jr 2006. Structurally controlled hydrothermal dolomite reservoir facies: an overview. *AAPG Bulletin*, **90**, 1641–1690, https://doi.org/10.1306/05220605164

Davison, I. 2007. Geology and tectonics of the South Atlantic Brazilian salt basins. *Geological Society, London, Special Publications*, **272**, 345–359, https://doi.org/10.1144/GSL.SP.2007.272.01.18

Dekov, V., Egueh, N. *et al*. 2014. Hydrothermal carbonate chimneys from a continental rift (Afar Rift): mineralogy, geochemistry, and mode of formation. *Chemical*

Geology, **387**, 87–100, https://doi.org/10.1016/j.chemgeo.2014.08.019

Dewit, J., Foubert, A., El Desouky, H., Muchez, P., Hunt, D., Vanhaecke, F. and Swennen, R. 2014. Characteristics, genesis and parameters controlling the development of a large stratabound HTD body at Matienzo (Ramales Platform, Basque–Cantabrian Basin, northern Spain). *Marine and Petroleum Geology*, **55**, 6–25, https://doi.org/10.1016/j.marpetgeo.2013.12.021

Dickson, J.A.D. 1965. A modified staining technique for carbonates in thin section. *Nature*, **205**, 587–587, https://doi.org/10.1038/205587a0

Eichhubl, P. and Boles, J.R. 2000. Rates of fluid flow in fault systems; evidence for episodic rapid fluid flow in the Miocene Monterey Formation, coastal California. *American Journal of Science*, **300**, 571–600, https://doi.org/10.2475/ajs.300.7.571

Everett, C., Wilkinson, J. and Rye, D. 1999. fracture-controlled fluid flow in the Lower Palaeozoic basement rocks of Ireland: implications for the genesis of Irish-type Zn–Pb Deposits. *Geological Society, London, Special Publications*, **155**, 247–276, https://doi.org/10.1144/GSL.SP.1999.155.01.18

Farias, F., Szatmari, P., Bahniuk, A. and Franca, A.B. 2019. Evaporitic carbonates in the pre-salt of Santos Basin – genesis and tectonic implications. *Marine and Petroleum Geology*, **105**, 251–272, https://doi.org/10.1016/j.marpetgeo.2019.04.020

Fetter, M. 2009. The role of basement tectonic reactivation on the structural evolution of Campos Basin, offshore Brazil: evidence from 3D seismic analysis and section restoration. *Marine and Petroleum Geology*, **26**, 873–886, https://doi.org/10.1016/j.marpetgeo.2008.06.005

Fetter, M., Penteado, H., Madrucci, V. and Spadini, A. 2018. The Paleogeography of the Lacustrine Rift System of the Pre-Salt in Santos Basin, Offshore Brazil. AAPG Search and Discovery article #11137. Adapted from an oral presentation given at the AAPG Annual Convention and Exhibition, Salt Lake City, Utah, 20–23 May 2018.

Ganade, C.E., Cioffi, C.R. *et al*. 2022. Recurrent tectonic activity in northeastern Brazil during Pangea breakup: constraints from U-Pb carbonate dating. *Geology*, **50**, 969–974, https://doi.org/10.1130/G50032.1

Goldstein, R.H. and Reynolds, T.J. 1994. Systematics of fluid inclusions in diagenetic minerals. *SEPM Short Course*, **31**.

Herlinger,, Jr R., Zambonato, E.E. and De Ros, L.F. 2017. Influence of diagenesis on the quality of Lower Cretaceous pre-salt lacustrine carbonate reservoirs from Northern Campos Basin, offshore Brazil. *Journal of Sedimentary Research*, **87**, 1285–1313, https://doi.org/10.2110/jsr.2017.70

Hesse, R. 1989. Silica diagenesis: origin of inorganic and replacement cherts. *Earth Science Reviews*, **26**, 253–284.

Hitzman, M.W. and Beaty, D.W. 1996. The Irish Zn-Pb-(Ba) Orefield. *In*: Sangster, D.F. (ed.) *Carbonate-Hosted Lead-Zinc Deposits: 75th Anniversary Volume*. Society of Economic Geologists, Special Publication, no. 4.

Hitzman, M.W., Redmond, P.B. and Beaty, D.W. 2002. The carbonate-hosted Lisheen Zn-Pb-Ag deposit, County Tipperary, Ireland. *Economic Geology*, **97**, 1627–1655, https://doi.org/10.2113/gsecongeo.97.8.1627

Hnatyshin, D., Creaser, R.A., Meffre, S., Stern, R.A., Wilkinson, J.J. and Turner, E.C. 2020. Understanding the microscale spatial distribution and mineralogical residency of Re in pyrite: examples from carbonate-hosted Zn-Pb ores and implications for pyrite Re-Os geochronology. *Chemical Geology*, **533**, 119 427, https://doi.org/10.1016/j.chemgeo.2019.119427

Hoefs, J. 1997. *Stable Isotope Geochemistry*, 8th edn. Springer.

Hollanda, M.H.B.M., Archanjo, C.J. *et al*. 2019. The Mesozoic Equatorial Atlantic Magmatic Province (EQUAMP): a new large igneous province in South America. *In*: Srivastava, R.K. (ed.) *Dyke Swarms of the World: A Modern Perspective*. Springer, Singapore, 87–110.

Immenhauser, A. 2022. On the delimitation of the carbonate burial realm. *The Depositional Record*, **8**, 524–574, https://doi.org/10.1002/dep2.173

Kelly, P., Peacock, D., Sanderson, D. and McGurk, A. 1999. Selective reverse-reactivation of normal faults, and deformation around reverse-reactivated faults in the Mesozoic of the Somerset coast. *Journal of Structural Geology*, **21**, 493–509, https://doi.org/10.1016/S0191-8141(99)00041-3

Klimchouk, A.B. 2012. Hypogene speleogenesis. *In*: White, W.B. and Colver, D.C. (eds) *Encyclopedia of Caves*, **945**. Elsevier Science and Technology, Amsterdam.

Klimchouk, A.B. 2015. The Karst Paradigm: Changes, Trends and Perspectives. *Acta Carsologica*, **44**, https://doi.org/10.3986/ac.v44i3.2996.

Kukla, P.A., Strozyk, F. and Mohriak, W.U. 2018. South Atlantic salt basins – witnesses of complex passive margin evolution. *Gondwana Research*, **53**, 41–57, https://doi.org/10.1016/j.gr.2017.03.012

Kyne, R., Torremans, K., Güven, J., Doyle, R. and Walsh, J. 2019. 3-D modeling of the Lisheen and Silvermines deposits, County Tipperary, Ireland: insights into structural controls on the formation of Irish Zn-Pb deposits. *Economic Geology*, **114**, 93–116, https://doi.org/10.5382/econgeo.2019.4621

Lander, R. and Laubach, S. 2015. Insights into rates of fracture growth and sealing from a model for quartz cementation in fractured sandstones. *Geological Society of America Bulletin*, **127**, 516–538, https://doi.org/10.1130/B31092.1

Laubach, S.E., Eichhubl, P., Hilgers, C. and Lander, R. 2010. Structural diagenesis. *Journal of Structural Geology*, **32**, 1866–1872, https://doi.org/10.1016/j.jsg.2010.10.001

Laubach, S.E., Lander, R. *et al*. 2019. The role of chemistry in fracture pattern development and opportunities to advance interpretations of geological materials. *Reviews of Geophysics*, **57**, 1065–1111, https://doi.org/10.1029/2019RG000671

Lawson, M., Sitgreaves, J. *et al*. 2022. New age and lake chemistry constraints on the Aptian pre-salt carbonates of the central South Atlantic. *GSA Bulletin*, **135**, 595–607, https://doi.org/10.1130/B36378.1

Leach, D.L., Sangster, D.F. *et al*. 2005. Sediment-hosted lead-zinc deposits: a global perspective. *Economic Geology*, **100**, 561–607, https://doi.org/10.5382/AV100.18

Lima, B.E.M. and De Ros, L.F. 2019. Deposition, diagenetic and hydrothermal processes in the Aptian Pre-Salt lacustrine carbonate reservoirs of the northern Campos Basin, offshore Brazil. *Sedimentary Geology*, **383**, 55–81, https://doi.org/10.1016/j.sedgeo.2019.01.006

Lima, B.E.M., Tedeschi, L.R., Pestilho, A.L.S., Santos, R.V., Vazquez, J.C., Guzzo, J.V.P. and De Ros, L.F. 2020. Deep-burial hydrothermal alteration of the Pre-Salt carbonate reservoirs from northern Campos Basin, offshore Brazil: evidence from petrography, fluid inclusions, Sr, C and O isotopes. *Marine and Petroleum Geology*, **113**, 104–143, http://doi.org/10.1016/j.marpetgeo.2019.104143

Loucks, R.G. 1999. Paleocave carbonate reservoirs: origins, burial-depth modifications, spatial complexity, and reservoir implications. *AAPG Bulletin*, **83**, 1795–1834.

Loucks, R.G., Mescher, P.K. and McMechan, G.A. 2004. Three-dimensional architecture of a coalesced, collapsed-paleocave system in the Lower Ordovician Ellenburger Group, central Texas. *AAPG Bulletin*, **88**, 545–564.

Machel, H.G. 1999. Effects of groundwater flow on mineral diagenesis, with emphasis on carbonate aquifers. *Hydrogeology Journal*, **7**, 94–107, https://doi.org/10.1007/s100400050182

Machel, H.G. 2001. Bacterial and thermochemical sulfate reduction in diagenetic settings – old and new insights. *Sedimentary Geology*, **140**, 143–175, https://doi.org/10.1016/S0037-0738(00)00176-7

Machel, H.G. and Lonnee, J. 2002. Hydrothermal dolomite – a product of poor definition and imagination. *Sedimentary Geology*, **152**, 163–171, https://doi.org/10.1016/S0037-0738(02)00259-2

Martín-Martín, J., Gomez-Rivas, E., Gómez-Gras, D., Travé, A., Ameneiro, R., Koehn, D. and Bons, P. 2018. Activation of stylolites as conduits for overpressured fluid flow in dolomitized platform carbonates. *Geological Society, London, Special Publications*, **459**, 157–176, https://doi.org/10.1144/SP459.3

Matos, R.M.D. 2021. Magmatism and hotspot trails during and after continental break-up in the South Atlantic. *Marine and Petroleum Geology*, **129**, 105 077, https://doi.org/10.1016/j.marpetgeo.2021.105077

Milani, E.J. and De Wit, M. 2008. Correlations between the classic Paraná and Cape–Karoo sequences of South America and southern Africa and their basin infills flanking the Gondwanides: du Toit revisited. *Geological Society, London, Special Publications*, **294**, 319–342, https://doi.org/10.1144/SP294.17

Miranda, T.S., Neves, S.P., Celestino, M.A.L., and Roberts, N.M.W. 2020. Structural evolution of the Cruzeiro do Nordeste shear zone (NE Brazil): Brasiliano-Pan-African ductile-to-brittle transition and Cretaceous brittle reactivation. *Journal of Structural Geology*, **141**, 104203, https://doi.org/10.1016/j.jsg.2020.104203

Mizusaki, A.M.P., Petrini, R., Bellieni, P., Comin-Chiaramonti, P., Dias, J., De Min, A. and Piccirillo, E.M. 1992. Basalt magmatism along the passive continental margin of SE Brazil (Campos basin). *Contributions to Mineralogy and Petrology*, **111**, 143–160, https://doi.org/10.1007/BF00348948

Mohriak, W., Nemčok, M. and Enciso, G. 2008. South Atlantic divergent margin evolution: rift-border uplift and salt tectonics in the basins of SE Brazil. *Geological Society, London, Special Publications*, **294**, 365–398, https://doi.org/10.1144/SP294.19

Morad, S., Ketzer, J. and De Ros, L.F. 2000. Spatial and temporal distribution of diagenetic alterations in siliciclastic rocks: implications for mass transfer in sedimentary basins. *Sedimentology*, **47**, 95–120, https://doi.org/10.1046/j.1365-3091.2000.00007.x

Morgan, J.P., Taramón, J.M., Araujo, M., Hasenclever, J. and Perez-Gussinye, M. 2020. Causes and consequences of asymmetric lateral plume flow during South Atlantic rifting. *Proceedings of the National Academy of Sciences*, **117**, 27 877–27 883, https://doi.org/10.1073/pnas.2012246117

Moulin, M., Aslanian, D. and Unternehr, P. 2010. A new starting point for the South and Equatorial Atlantic Ocean. *Earth-Science Reviews*, **98**, 1–37, https://doi.org/10.1016/j.earscirev.2009.08.001

Muniz, M.C. and Bosence, D.W.J. 2015. Pre-salt microbialites from the Campos Basin (offshore Brazil): image log facies, facies model and cyclicity in lacustrine carbonates. *Geological Society, London, Special Publications*, **418**, 221–242, https://doi.org/10.1144/SP418.10

Naden, J. 1996. *CalcicBrine*: a Microsoft Excel 5.0 add-in for calculating salinities from microthermometric data in the system NaCl–$CaCl_2$–H_2O. PACROFI VI, Madison, WI, University of Wisconsin.

Neilson, J. and Oxtoby, N. 2008. The relationship between petroleum, exotic cements and reservoir quality in carbonates – a review. *Marine and Petroleum Geology*, **25**, 778–790, https://doi.org/10.1016/j.marpetgeo.2008.02.004

Oakes, C.S., Bodnar, R.J. and Simonson, J.M. 1990. The system NaCl-$CaCl_2$-H_2O: I. The ice liquidus at 1 atm total pressure. *Geochimica et Cosmochimica Acta*, **54**, 603–610, https://doi.org/10.1016/0016-7037(90)90356-P

Olivito, J.P.R. and Souza, F.J. 2020. Depositional model of early Cretaceous lacustrine carbonate reservoirs of the Coqueiros formation - Northern Campos Basin, southeastern Brazil. *Marine and Petroleum Geology*, **111**, 414–439, https://doi.org/10.1016/j.marpetgeo.2019.07.013

Paarlberg, N. and Evans, L. 1977. Geology of the Fletcher Mine, Viburnum Trend, Southeast Missouri. *Economic Geology*, **72**, 391–397, https://doi.org/10.2113/gsecongeo.72.3.391

Packard, J.J., Al-Aasm, I., Samson, I., Berger, Z. and Davies, J. 2001. A Devonian hydrothermal chert reservoir: the 225 bcf Parkland field, British Columbia, Canada. *AAPG Bulletin*, **85**, 51–84, https://doi.org/10.1306/8626C75D-173B-11D7-8645000102C1865D

Parise, M., Gabrovsek, F., Kaufmann, G. and Ravbar, N. 2018. Recent advances in karst research: from theory to fieldwork and applications. *Geological Society, London, Special Publications*, **466**, 1–24, https://doi.org/10.1144/SP466.26

Pietzsch, R., Oliveira, D.M., Tedeschi, L.R., Neto, J.V.Q., Figueiredo, M.F., Vazquez, J.C. and Souza, R.S. 2018. Palaeohydrology of the Lower Cretaceous pre-salt lacustrine system, from rift to post-rift phase, Santos

Basin, Brazil. *Palaeogeography, Palaeoclimatology, Palaeoecology*, **507**, 60–80, https://doi.org/10.1016/j.palaeo.2018.06.043

Pietzsch, R., Tedeschi, L.R., Oliveira, D.M., dos Anjos, C.W.D., Vazquez, J.C. and Figueiredo, M.F. 2020. Environmental conditions of deposition of the Lower Cretaceous lacustrine carbonates of the Barra Velha Formation, Santos Basin (Brazil), based on stable carbon and oxygen isotopes: a continental record of pCO_2 during the onset of the Oceanic Anoxic Event 1a (OAE 1a) interval? *Chemical Geology*, **535**, https://doi.org/10.1016/j.chemgeo.2019.119457

Pingitore, N.E. 1982. The role of diffusion during carbonate diagenesis. *Journal of Sedimentary Research*, **52**, 27–39.

Preibisch, S., Saalfeld, S. and Tomancak, P. 2009. Globally optimal stitching of tiled 3D microscopic image acquisitions. *Bioinformatics*, **25**, 1463–1465, https://doi.org/10.1093/bioinformatics/btp184

Rabinowitz, P.D. and LaBrecque, J. 1979. The Mesozoic South Atlantic Ocean and evolution of its continental margins. *Journal of Geophysical Research*, **84**, 5973–6002, https://doi.org/10.1029/JB084iB11p05973

Roberts, N.M.W. and Walker, R.J. 2016. U-Pb geochronology of calcite-mineralized faults: absolute timing of rift-related fault events on the northeast Atlantic margin. *Geology*, **44**, 531–534, https://doi.org/10.1130/G37868.1

Roberts, N.M.W., Rasbury, E.T., Parrish, R.R., Smith, C.J., Horstwood, M.S.A. and Condon, D.J. 2017. A calcite reference material for La-Icp-Ms U-Pb geochronology. *Geochemistry, Geophysics, Geosystems*, **18**, 2807–2814, https://doi.org/10.1002/2016GC006784

Roberts, N.M.W., Drost, K. *et al*. 2020. Laser ablation inductively coupled plasma mass spectrometry (LA-ICP-MS) U–Pb carbonate geochronology: strategies, progress, and limitations. *Geochronology*, **2**, 33–61, https://doi.org/10.5194/gchron-2-33-2020

Rocha, B.C., Davies, J.H.F.L. *et al*. 2020. Rapid eruption of silicic magmas from the Paraná magmatic province (Brazil) did not trigger the Valanginian event. *Geology*, **48**, 1174–1178, https://doi.org/10.1130/G47766.1

Rochelle-Bates, N., Roberts, N. *et al*. 2021. Geochronology of volcanically associated hydrocarbon charge in the pre-salt carbonates of the Namibe Basin, Angola. *Geology*, **49**, 335–340, https://doi.org/10.1130/G48019.1

Rochelle-Bates, N., Wood, R., Schröder, S. and Roberts, N.M.W. 2022. In situ U–Pb geochronology of Pre-Salt carbonates reveals links between diagenesis and regional tectonics. *Terra Nova*, **34**, 271–277, https://doi.org/10.1111/ter.12586

Roedder, E. 1984. *Fluid Inclusions*. Mineralogical Society of America, Reviews in Mineralogy, **12**.

Sanjinés, A.E.S., Viviers, M.C., Costa, D.S., dos Anjos Zerfass, G.d.S., Beurlen, G. and Strohschoen, O., Jr. 2022. Planktonic foraminifera from the Aptian section of the Southeastern Brazilian Atlantic margin. *Cretaceous Research*, **134**, 105–141, https://doi.org/10.1016/j.cretres.2022.105141

Santiago, R., de Andrade Caxito, F., Neves, M.A., Dantas, E.L., de Medeiros Júnior, E.B. and Queiroga, G.N. 2020. Two generations of mafic dyke swarms in the Southeastern Brazilian coast: reactivation of structural lineaments during the gravitational collapse of the Araçuaí-Ribeira Orogen (500 Ma) and West Gondwana Breakup (140 Ma). *Precambrian Research*, **340**, https://doi.org/10.1016/j.precamres.2019.105344

Schmitt, R.S., Trouw, R.A.J., Van Schmus, W.R. and Pimentel, M.M. 2004. Late amalgamation in the central part of West Gondwana: new geochronological data and the characterization of a Cambrian collisional orogeny in the Ribeira Belt (SE Brazil). *Precambrian Research*, **133**, 29–61, https://doi.org/10.1016/j.precamres.2004.03.010

Schmitt, R.S., Trouw, R., Van Schmus, W.R., Armstrong, R. and Stanton, N.S.G. 2016. The tectonic significance of the Cabo Frio Tectonic Domain in the SE Brazilian margin: a Paleoproterozoic through Cretaceous saga of a reworked continental margin. *Brazilian Journal of Geology*, **46**, 37–66, https://doi.org/10.1590/2317-4889201620150025

Sibson, R.H. 1981. Fluid flow accompanying faulting: field evidence and models. *In*: Simpson, P.G.R.D.W. (ed.) *Earthquake Prediction: an international review*, **4**. American Geophysical Union, 593–603.

Sibson, R.H. 1992. Fault-valve behavior and the hydrostatic-lithostatic fluid pressure interface. *Earth-Science Reviews*, **32**, 141–144, https://doi.org/10.1016/0012-8252(92)90019-P

Stanton, N., Kusznir, N., Gordon, A. and Schmitt, R.S. 2019. Architecture and Tectono-magmatic evolution of the Campos Rifted Margin: control of OCT structure by basement inheritance. *Marine and Petroleum Geology*, **100**, 43–59, https://doi.org/10.1016/j.marpetgeo.2018.10.043

Strugale, M., Schmitt, R.S. and Cartwright, J. 2021. Basement geology and its controls on the nucleation and growth of rift faults in the northern Campos Basin, offshore Brazil. *Basin Research*, **33**, 1906–1933, https://doi.org/10.1111/bre.12540

Strugale, M. and Cartwright, J.A. 2022. Tectono-stratigraphic evolution of the rift and post-rift systems in the Northern Campos Basin, offshore Brazil. *Basin Research*, **34**, 1655–1687, https://doi.org/10.1111/bre.12674

Szatmari, P., de Lima, C.M. *et al*. 2021. Petrography, geochemistry and origin of South Atlantic evaporites: the Brazilian side. *Marine and Petroleum Geology*, **127**, 104 805, https://doi.org/10.1016/j.marpetgeo.2020.104805

Tedeschi, L.R., Jenkyns, H.C., Robinson, S.A., Sanjinés, A.E.S., Viviers, M.C., Quintaes, C.M.S.P. and Vazquez, J.C. 2017. New age constraints on Aptian evaporites and carbonates from the South Atlantic: implications for Oceanic Anoxic Event 1a. *Geology*, **45**, 543–546, https://doi.org/10.1130/G38886.1

Tedeschi, L.R., Jenkyns, H.C., Robinson, S.A., Lana, C.C., Menezes Santos, M.R.F. and Tognoli, F.M.W. 2019. Aptian carbon-isotope record from the Sergipe-Alagoas Basin: new insights into oceanic anoxic event 1a and the timing of seawater entry into the South Atlantic. *Newsletters on Stratigraphy*, **53**, 333–364, https://doi.org/10.1127/nos/2019/0529

Thomas Filho, A., Mizusaki, A.M.P., Milani, E.J. and Cesero, P. 2000. Rifting and magmatism associated with the South America and Africa Breakup. *Brazilian Journal of Geology*, **30**, 17–19.

Tritlla, J., Loma, R. *et al*. 2018. Pre-Salt Lacustrine Carbonates, Diagenetic Silicification and Hydrothermal Overprinting in Kwanza Basin (Offshore Angola): A Tale of Two Silicas. Paper presented at the AAPG Annual Conference and Exhibition, Salt Lake City, Utah, 20–23 May 2018.

Turner, J.P. and Williams, G.A. 2004. Sedimentary basin inversion and intra-plate shortening. *Earth-Science Reviews*, **65**, 277–304, https://doi.org/10.1016/j.earscirev.2003.10.002

Vieira de Luca, P.H., Matias, H. *et al*. 2017. Breaking barriers and paradigms in presalt exploration: the Pão De Açúcar Discovery (offshore Brazil). *In*: Merrill, R.K. and Sternbach, C.A. (eds) *Giant Fields of the Decade 2000–2010*. AAPG Memoir, **113**, https://doi.org/10.1306/13572007M1133686

Walsh, J.J., Torremans, K., Güven, J., Kyne, R., Conneally, J. and Bonson, C. 2018. Fault-controlled fluid flow within extensional basins and its implications for sedimentary rock-hosted mineral deposits. *In*: Arribas, A.M.R. and Mauk, J.L. (eds) *Metals, Minerals, and Society*. Society of Economic Geologists, **21**, https://doi.org/10.5382/SP.21.11

Warren, J. 2000. Dolomite: occurrence, evolution and economically important associations. *Earth-Science Reviews*, **52**, 1–81, https://doi.org/10.1016/S0012-8252(00)00022-2

White, D.E. 1957. Thermal waters of volcanic origin. *GSA Bulletin*, **68**, 1637–1658, https://doi.org/10.1130/0016-7606(1957)68[1637:TWOVO]2.0.CO;2

Wilkinson, J.J., Eyre, S.L. and Boyce, A.J. 2005. Ore-forming processes in Irish-type carbonate-hosted Zn-Pb deposits: evidence from mineralogy, chemistry, and isotopic composition of sulfides at the Lisheen Mine. *Economic Geology*, **100**, 63–86, https://doi.org/10.2113/100.1.0063

Winter, W.R., Jahnert, R.J. and França, A.B. 2007. Bacia e Campos. *Boletim de Geociências da Petrobras*, **15**, 511–529.